Third Radiation Transfer Model Intercomparison (RAMI) exercise: Documenting progress in canopy reflectance models

J.-L. Widlowski,[1] M. Taberner,[1] B. Pinty,[1] V. Bruniquel-Pinel,[2] M. Disney,[3,4] R. Fernandes,[5] J.-P. Gastellu-Etchegorry,[6] N. Gobron,[1] A. Kuusk,[7] T. Lavergne,[1] S. Leblanc,[8] P. E. Lewis,[3,4] E. Martin,[6] M. Mõttus,[7] P. R. J. North,[9] W. Qin,[10] M. Robustelli,[1] N. Rochdi,[5] R. Ruiloba,[2] C. Soler,[11] R. Thompson,[12] W. Verhoef,[13] M. M. Verstraete,[1] and D. Xie[14]

Received 24 July 2006; revised 7 November 2006; accepted 29 November 2006; published 8 May 2007.

[1] The Radiation Transfer Model Intercomparison (RAMI) initiative benchmarks canopy reflectance models under well-controlled experimental conditions. Launched for the first time in 1999, this triennial community exercise encourages the systematic evaluation of canopy reflectance models on a voluntary basis. The first phase of RAMI focused on documenting the spread among radiative transfer (RT) simulations over a small set of primarily 1-D canopies. The second phase expanded the scope to include structurally complex 3-D plant architectures with and without background topography. Here sometimes significant discrepancies were noted which effectively prevented the definition of a reliable "surrogate truth," over heterogeneous vegetation canopies, against which other RT models could then be compared. The present paper documents the outcome of the third phase of RAMI, highlighting both the significant progress that has been made in terms of model agreement since RAMI-2 and the capability of/need for RT models to accurately reproduce local estimates of radiative quantities under conditions that are reminiscent of in situ measurements. Our assessment of the self-consistency and the relative and absolute performance of 3-D Monte Carlo models in RAMI-3 supports their usage in the generation of a "surrogate truth" for all RAMI test cases. This development then leads (1) to the presentation of the "RAMI Online Model Checker" (ROMC), an open-access web-based interface to evaluate RT models automatically, and (2) to a reassessment of the role, scope, and opportunities of the RAMI project in the future.

Citation: Widlowski, J.-L., et al. (2007), Third Radiation Transfer Model Intercomparison (RAMI) exercise: Documenting progress in canopy reflectance models, *J. Geophys. Res.*, *112*, D09111, doi:10.1029/2006JD007821.

[1]Global Environment Monitoring Unit, Institute for Environment and Sustainability, European Commission–DG Joint Research Centre, Ispra, Italy.
[2]NOVELTIS, Ramonville Saint-Agne, France.
[3]Department of Geography, University College London, London, UK.
[4]Also at Centre for Terrestrial Carbon Dynamics, Natural Environment Research Council, London, UK.
[5]Canada Centre for Remote Sensing, Natural Resources Canada, Ottawa, Ontario, Canada.
[6]Centre d'Etudes Spatiales de la Biosphère, Toulouse, France.
[7]Tartu Observatory, Tõravere, Estonia.
[8]Centre Spatial John H. Chapman, Saint-Huber, Québec, Canada.
[9]Climate and Land-Surface Systems Interaction Centre, Department of Geography, University of Wales, Swansea, UK.
[10]Science Systems and Applications, Inc., Lanham, Maryland, USA.
[11]Acquisition, Representation and Transformations for Image Synthesis, Institut National de Recherche en Informatique et en Automatique Rhône-Alpes, Saint Ismier, France.
[12]Alachua Research Institute, Alachua, Florida, USA.
[13]National Aerospace Laboratory NLR, Emmeloord, Netherlands.
[14]Research Center for Remote Sensing and GIS, School of Geography, Beijing Normal University, Beijing, China.

0148-0227/07/2006JD007821

1. Introduction

[2] Spaceborne observations constitute a highly appropriate source of information to quantify and monitor Earth surface processes. The quality/confidence that may be associated with the outcome of interpretation and assimilation efforts of these data streams, however, relies heavily on the actual performance of the available modeling tools. This understanding has led to a series of model intercomparison projects (MIP) aiming either to document the spread of currently available simulation models, or, else to assess and benchmark the quality of their simulation results [e.g., *Henderson-Sellers et al.*, 1995; *Gates et al.*, 1998; *Dirmeyer et al.*, 1999; *Pinty et al.*, 2001; *Latif et al.*, 2001; *Cahalan et al.*, 2005; *Halthore et al.*, 2005]. Among these MIPs the RAdiation transfer Model Intercomparison (RAMI) activity focuses on the proper representation of the radiative processes occurring, in vegetated environments, in the optical domain of the solar spectrum. The design and launch of the first phase of RAMI occurred approximately in parallel with that of the "Intercomparison of 3-D Radiation Codes"

(I3RC) activity which deals with the correct representation of the radiative properties of 3-D cloud fields (http://i3rc.gsfc.nasa.gov/). Both MIPs collaborate actively and share their evaluation methodologies in order to overcome the difficulties associated with model benchmarking in the absence of absolute reference standards.

[3] The first phase of RAMI (RAMI-1) was launched in 1999. Its prime objective was to document the variability that existed between canopy reflectance models when run under well controlled experimental conditions [*Pinty et al.*, 2001]. The positive response of the various RAMI-1 participants and the subsequent improvements made to a series of radiative transfer (RT) models promoted the launching of the second phase of RAMI (RAMI-2) in 2002. Here the number of test cases was expanded to focus further on the performance of models dealing with structurally complex 3-D plant environments. The main outcomes of RAMI-2 included (1) an increase in the number of participating models, (2) a better agreement between the model simulations in the case of the structurally simple scenes inherited from RAMI-1, and (3) the need to reduce the sometimes substantial differences between some of the 3-D RT models over complex heterogeneous scenes [*Pinty et al.*, 2004b]. The latter issue was noted as one of the challenges that future intercomparison activities would have to face, since the reliable derivation of some sort of "surrogate truth" data set will not be possible in the absence of any agreement between these RT models. This, in turn, would then imply that except in some simple special cases, the evaluation of RT model simulations cannot proceed beyond their mutual comparison because of the general lack of absolute reference standards.

[4] This paper will describe the outcome of the third phase of RAMI (RAMI-3). Section 2 will provide an overview of the organization and model evaluation protocol employed during RAMI-3. Section 3 documents how the performance of RT models, when applied to the various baseline scenarios inherited from RAMI-1, improved between RAMI-2 and RAMI-3. Section 4 documents the outcome of model simulations for the newly proposed experiments and measurement types in RAMI-3. Section 5 summarizes the main achievements and issues observed during RAMI-3 and introduces the "Rami Online Model Checker" (ROMC), a web-based tool intended to automate the process of RT model benchmarking. Section 5 also describes possible roadmaps for the future development of the RAMI initiative.

2. Third Phase of RAMI

[5] The third phase of RAMI was officially launched at the end of March 2005. Scientists from around the world with an interest in canopy RT modeling were invited to participate in this triennial benchmarking exercise. A dedicated Web site (http://rami-benchmark.jrc.it/) provided detailed descriptions regarding the structural, spectral and illumination conditions of the test cases proposed for RAMI-3. Note that because of a renaming of all European Commission Web sites this URL is likely to change in the near future to http://rami-benchmark.jrc.ec.europa.eu/. Prior to going public, each one of these experiments and measurements had been approved by the RAMI advisory body, a small group of well-known scientists in the field of radiative transfer modeling and/or model intercomparison activities. RAMI-3 included and built upon the various experiments and measurements proposed during earlier phases of RAMI [see *Pinty et al.*, 2001, section 2.1; *Pinty et al.*, 2004b, section 2]. Overall, the number of simulation scenarios grew by 37% with respect to RAMI-2, which led to two separate submission deadlines, namely, 30 July 2005 for all RT simulations pertaining to structurally homogeneous vegetation canopies and 15 December 2005 for all those simulations relating to structurally heterogeneous test cases. As was the case during previous phases of RAMI, the collection of the submitted RT model results and their detailed analysis were performed at the Joint Research Centre (JRC) of the European Commission in Ispra, Italy. Two public presentations describing the outcome of this community effort were delivered, the first one, dealing with homogeneous test cases only, was given during the 9th International Symposium on Physical Measurements and Signatures in Remote Sensing (ISPMSRS) in Beijing, China (October 2005), and the second one, including also the heterogeneous test cases, at the 4th International workshop on multiangular measurements and models (IWMMM-4) in Sydney, Australia (March 2006).

[6] Table 1 lists the models that participated in RAMI-3, the main publications describing these models and the names and affiliations of their operators. Also indicated are the corresponding modeling approaches that are used in order to simulate the radiation transfer. These include Monte Carlo (MC) techniques associated with forward/reverse ray-tracing methods (Drat, FLIGHT, frat, raytran, Rayspread and Sprint3) or radiosity approaches (RGM and Hyemalis), purely analytical formulations (2-Stream), as well as a large number of hybrid techniques, that combine one or more of the above with numerical, stochastic and/or geometric optical approaches (ACRM, DART, 1/2-discret, FRT, MAC, MBRF, Sail++, 4SAIL2, 5Scale). More detailed information on the participating models can be found on the RAMI Web site under http://rami-benchmark.jrc.it/HTML/RAMI3/MODELS/MODELS.php. Most of the participants received substantial feedback on the performance of their model(s) both as a result of phases 1 and 2, and in the case of obvious errors/deviations also during phase 3 of RAMI. Consequently, all results presented below refer to the latest and most up-to-date version of these models. It is important that prospective users of these models ensure that they have access to the most recent version of these codes, as the performance information provided here may not be representative of, or applicable to, earlier versions.

[7] One of the traits of RAMI is to increase the number of test cases by including a few new experiments (and measurements) from one phase to another. This strategy serves a dual purpose, namely, (1) to allow the evaluation of RT models under an increasingly comprehensive set of structural, spectral and also illumination conditions and (2) to tailor new sets of RAMI experiments and measurements around scientific questions emerging in the context of RT modeling and the quantitative interpretation of remotely sensed data. Indeed, such an approach guarantees that every phase will contain at least some test cases for which the simulation results cannot be known a priori. Within RAMI-3 the following new experiments were proposed: (1) a conser-

Table 1. List of the Participating Models, Their RT Implementation Type, Scene Construction Approach and Main Scientific Reference, as Well as the Names of Their Operators During RAMI-3[a]

Model Name	RT Formalism	Scene Setup	Reference	Participant
1-D models				
ACRM	analytic + MKC	2-layer PP, SD	*Kuusk* [2001]	A. Kuusk[b]
MBRF	analytic + hot spot kernel	PP, SD	*Qin and Xiang* [1997]	W. Qin[c]
Sail++	N+2 stream	PP, SD	*Verhoef* [1998, 2002]	W. Verhoef[d]
1/2-discret	analytic + DOM	PP, SD	*Gobron et al.* [1997]	N. Gobron[e]
2-Stream	analytic	PP, SD	*Pinty et al.* [2006]	T. Lavergne[e]
3-D models				
5Scale	hybrid (GO)	GP, SD	*Leblanc and Chen* [2001]	N. Rochdi[f] and S. Leblanc[g]
FLIGHT	MC,RT (forward/reverse)	GP, DL or SD	*North* [1996]	P. North[h]
4SAIL2	hybrid (4 stream + GO)	2-layer PG,FC	*Verhoef and Bach* [2003]	W. Verhoef[d]
frat	MC,RT (forward)	GP, DL	unpublished	P. Lewis[i] and M. Disney[i]
FRT	hybrid (GO)	GP, SD	*Kuusk and Nilson* [2000]	M. Mõttus[b] and A. Kuusk[b]
DART	RT (forward) + DOM	voxels, SD	*Gastellu-Etchegorry et al.* [1996, 2004]	E. Martin[j] and J.-P. Gastellu[j]
Drat	MC,RT (reverse)	GP, DL	*Lewis* [1999] and *Saich et al.* [2001]	P. Lewis[i] and M. Disney[i]
Hyemalis	radiosity approach	GP, OP, DL	*Soler and Sillion* [2000] and *Helbert et al.* [2003]	R. Ruiloba,[k] C. Soler,[l] and V. Bruniquel-Pinel[k]
MAC	hybrid (GO)	GP, SD, FC	*Fernandes et al.* [2003]	R. Fernandes[f] and N. Rochdi[f]
Rayspread	MC,RT (forward + VR)	GP, DL or SD	*Widlowski et al.* [2006a]	T. Lavergne[e]
raytran	MC,RT (forward)	GP, DL or SD	*Govaerts and Verstraete* [1998]	T. Lavergne[e]
RGM	radiosity	GP, DL	*Qin and Gerstl* [2000]	D. Xie[m]
Sprint3	MC,RT (forward + VR)	GP, SD	*Thompson and Goel* [1998]	R. Thompson[n]

[a]DL means deterministic location of scatterer, DOM means discrete ordinate method, FC means statistical description of foliage clumping, GO means geometric optics, GP means geometric primitives, MC means Monte Carlo approach, MKC means Markov chain, OP means optic primitive, PP means plane parallel canopy, PG means parametric description of canopy gaps, RT means ray-tracing scheme, SD means statistical distribution of scatterer, and VR means variance reduction technique.
[b]Tartu Observatory, Tõravere.
[c]Science Systems and Applications, Inc., Greenbelt, Maryland.
[d]National Aerospace Laboratory NLR.
[e]Joint Research Centre.
[f]Canada Centre for Remote Sensing, Ottawa.
[g]Centre Spatial John H. Chapman, Saint-Huber, Québec.
[h]NERC CLASSIC, University of Wales Swansea.
[i]Department of Geography, University College London.
[j]Centre d'Etudes Spatiales de la Biosphère.
[k]NOVELTIS, France.
[l]ARTIS, INRIA, Rhône-Alpes, France.
[m]School of Geography, Beijing Normal University.
[n]Alachua Research Institute.

vative scattering scenario for the heterogeneous ''floating spheres'' test cases originally introduced during RAMI-1; (2) a ''coniferous forest'' scene analogous to the Gaussian-hill canopy introduced during RAMI-2 but without the topography; and (3) a ''birch stand'' populated with trees of variable sizes and spectral properties, intended primarily to enhance the degree of structural realism amongst the RAMI test cases. The new experiments complement those introduced during earlier phases of RAMI, which focused primarily on structurally homogeneous vegetation canopies (both in the solar domain and under conservative scattering conditions) but included also a small set of structurally heterogeneous plant canopies [see *Pinty et al.*, 2001, section 2.1; *Pinty et al.*, 2004b, section 2]. Exhaustive documentation on the spectral and structural properties of the various plant canopies (including the exact position and orientation of individual leaves in the scenes with discrete foliage representations, as well as the precise location of all tree-like objects in the scene) were accessible to the participants via the RAMI Web site. It was, however, left to the participants themselves to choose what level of detail their model required in order to represent at best the proposed canopy scenes.

[8] Similar to previous phases of RAMI, participants were encouraged to generate a standard set of 11 measurements for every test case. These measurements include the total spectral Bidirectional Reflectance Factor (BRF), in both the principal and the cross plane, together with the corresponding contributions due to the single-uncollided radiation scattered once by the soil only, the single-collided radiation by the leaves or trees only, and the radiation multiply collided by the leaves/trees/soil system. Three flux quantities were also routinely asked for, namely, the spectral albedo of the canopy (i.e., the directional hemispherical reflectance), the total transmission down to the underlying background, and, the total absorption of radiation in the vegetation layer. In addition to these standard measurements, RAMI-3 introduced two new measurement types, that applied, however, only to selected test cases. The first of these was a local transmission transect measurement that was asked for the ''birch stand'' experiment in order to assess the ability of RT models to simulate in situ measurement situations. Similarly, a horizontal flux measurement was proposed for the ''real-zoom-in'' scene, that was first introduced during RAMI-2 [*Pinty et al.*, 2004b, section 2.2], in order to document the performance of RT models when estimating the magnitude of horizontal photon transport at various spatial resolutions in a structurally heterogeneous canopy environment. Almost all the RAMI measurements, whether directional or hemispherical, had to be carried out

with respect to a reference plane located at the top of canopy height level.

[9] Overall a total of 464,816 (2,112) individual BRF (flux) simulations were received at the JRC. In order to pursue the analysis of these data beyond a mere visual comparison a protocol is needed that permits the quantitative evaluation of RT model simulations despite the lack of absolute reference standards (i.e., in general the true solution is not known). *Oreskes et al.* [1994], and many others since, maintain that under these latter conditions, the complete validation/verification of a model is quite impossible, and that any such endeavor should focus instead on showing the opposite, that is, the onset of flaws in a model's behavior. RAMI thus proposes a three-step procedure to identify incongruous RT models: (1) by assessing the absence of inconsistencies in the internal RT formulation of a model, (2) by verifying the accurate and reliable performance of a model in the limited number of cases where analytical solutions are available, and (3) by comparing the output of a model against a "surrogate truth" that is to be established from credible candidates within the ensemble of available RT simulations. Obviously the latter will only be meaningful if sufficient consensus exists among the simulation results of RT models, in particular those that are known to minimize the number of simplifications/approximations in their radiative transfer formulation. The objective of this three-step procedure thus lies in identifying RT models that deviate from the norm rather than boosting the credibility of those models that do not differ. In fact, conformity with the anticipated outcome in each one of the above steps is not proof of a model's physical correctness. Hence any claims regarding the credibility of a model's performance should be avoided, or, if they have to be made, should always be limited to the set of prescribed conditions under which the models were actually tested.

[10] In general, RT simulation models are rarely completely amiss, nor, totally correct for that matter, but tend to lie somewhere in between these two extremes. The quality of their simulations is often subject to the degree by which a given set of experimental conditions satisfies the structural, spectral and/or radiative premises on which the models are based. In the context of RAMI, for example, models often do not share the same internal representation or "image" of the prescribed canopy structure. (Canopy structure is defined here as the (statistical or deterministic) description of locations and orientations of foliage and woody constituents within the three-dimensional space of a RAMI scene.) Such architectural deviations may often form the basis for subsequent differences in simulation results, as will be seen in sections 3 and 4. In addition to possible (structure and illumination related) differences in the starting premises of RT models, the precise manner in which certain RT quantities are simulated may also vary, e.g., the width of the solid angle over which BRFs are computed may vary. The identification of suitable limits describing the threshold between valid and invalid models thus has to account for these idiosyncrasies, and should preferably be formulated in conjunction with criteria relating to the usage of these models. For example, by incorporating the absolute calibration accuracy of current space borne sensors and/or the anticipated quality of state-of-the-art atmospheric correction schemes into the evaluation scheme. In the next section the above three-step invalidation procedure will be applied to an ensemble of RAMI test cases for which analytical solutions are available in a few isolated cases, and so-called "surrogate truths" may be derived for others [e.g., *Pinty et al.*, 2001, 2004b].

3. RAMI Baseline Scenarios

[11] All the forward mode experiments that were proposed during RAMI-1 have featured in subsequent phases of the RAMI activity. These "baseline scenarios" can be subdivided into two separate architectural classes: The first one consists of structurally homogeneous canopies that feature finite-sized (discrete) or point-like (turbid) foliage elements that are randomly distributed within the volume of a horizontally infinite vegetation layer bounded by some top-of-canopy (TOC) level, as well as a lower flat background surface. The second category relates to structurally heterogeneous "floating spheres" environments where the (discrete or turbid) foliage elements are randomly distributed within a series of spherical volumes that are themselves freely floating above an underlying flat background surface (for a graphical depiction see the inlaid pictures in Figure 1). In both categories the directional scattering properties of the foliage and background are Lambertian, and the orientation of the foliage elements follow predefined leaf normal distributions (LND) [i.e., *Bunnik*, 1978; *Goel and Strebel*, 1984]. By varying the illumination conditions, as well as the number, size, orientation and spectral properties of the foliage elements in the canopy (idem for the background brightness) up to 52 structurally homogeneous and 8 "floating spheres" baseline scenarios were defined. In the structurally homogeneous case, a "purist corner" was included where the spectral leaf and soil properties are such as to test model performance in the limit of conservative scattering conditions, i.e., the soil brightness ($\alpha = 1$) and the single-scattering albedo ($r_L + t_L = 1$) are unity, and the leaf reflectance (r_L) is equal to the leaf transmittance (t_L).

[12] Figure 1 provides examples of the spread between the various RT models that participated in the baseline scenarios during RAMI-3. Shown are bidirectional reflectance factor (BRF) simulations along the principal (Figures 1a and 1c) and orthogonal (Figures 1b and 1d) planes for structurally homogeneous (Figures 1a and 1b) and heterogeneous "floating spheres" (Figures 1c and 1d) canopies. Figures 1a and 1c feature finite-sized disc-shaped foliage elements of infinitesimal thickness (radius 0.1 m), whereas Figures 1c and 1d relate to turbid medium canopies, i.e., having infinitesimally small but oriented scatterers. The spectral properties of the canopy constituents in Figures 1a and 1c (Figures 1b and 1d) are typical for vegetation and bare soils in the red (NIR) spectral domain. The illumination zenith angle (θ_i) was set to 20° in all these cases. The panels of Figure 1 exemplify the degree and variability of agreement between the various participating models. In particular, in the case of the structurally homogeneous test cases it is only the BRF simulations of the MBRF model in the turbid medium case (Figure 1b), and, to a lesser extent, the ACRM model in the discrete case (Figure 1a) that are different. The deviations of the MBRF

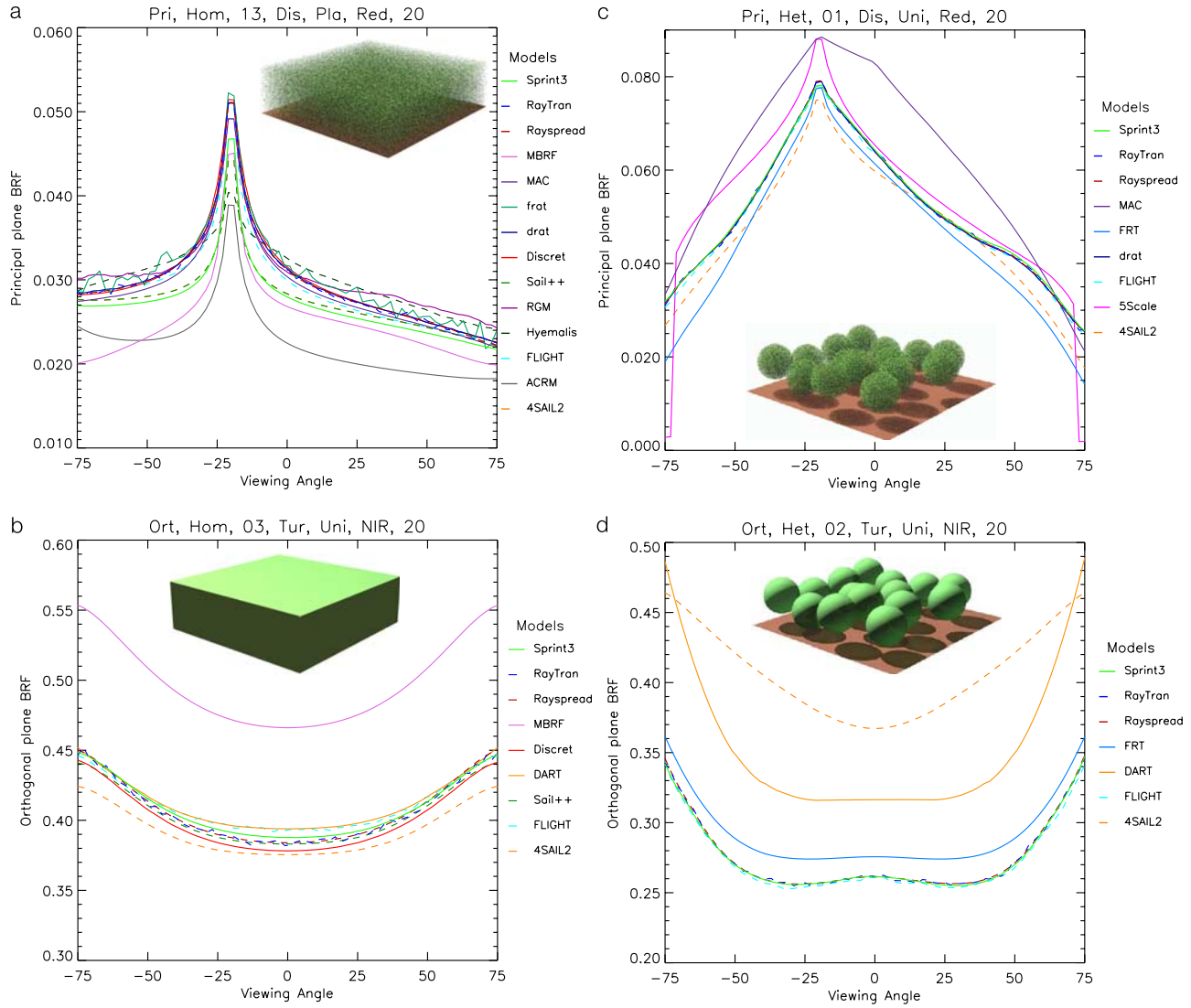

Figure 1. Sample BRF results for (a and b) structurally homogeneous and (c and d) "floating spheres" canopies. In Figures 1a and 1c, model simulations along the principal plane relate to test cases with finite-sized scatterers and spectral properties that are typical of the red spectral band. In Figures 1b and 1d, those along the orthogonal plane relate to turbid medium foliage representations with spectral properties that are typical of the near-infrared (NIR). The illumination zenith angle was 20° in all cases. Also shown are graphical representations of the various canopy structures.

model in the NIR may be largely explained by its usage of a "two-stream" approximation when estimating the multiple collided BRF component. At the same time the agreement between the FLIGHT, drat, Rayspread, raytran, and Sprint3 Monte Carlo models is striking for both the homogeneous and heterogeneous test cases. Somewhat different from these 5 models, and each other, are the simulation results for DART, MAC, FRT, 4SAIL2, and 5Scale in the turbid and/or discrete "floating spheres" test cases.

[13] Despite the visually noticeable dispersion of some of the model contributions in Figure 1, one should, in general, refrain from speculative guesses about potential outliers without a careful examination of the exact conditions under which the various models were executed. One of the first aspects to verify is the faithful representation of the prescribed architectural canopy characteristics. It is now well accepted that multiangular observations are sensitive to the structure of a given canopy target [e.g., *Gerard and North*, 1997; *Widlowski et al.*, 2001; *Lovell and Graetz*, 2002; *Chopping et al.*, 2003; *Chen et al.*, 2003; *Rautiainen et al.*, 2003]. By the same token, deviations from the structural characteristics of a given RAMI scene may thus translate itself into the model-simulated magnitude (and shape) of the TOC BRF field. During RAMI-3 almost all of the participating models differed in their structural premises, either systematically or occasionally, from those prescribed on the RAMI Web site. For example, the ACRM and MBRF models both use elliptical equations [*Campbell*, 1990] rather than beta-functions or geometric formulations to describe the LNDs of the foliage elements; DART approximates the "floating spheres" by a series of small cubes; Hyemalis reduced the physical dimensions of the proposed scenes to

deal with internal computer memory requirements; MAC, FRT and 5Scale assume a statistical, that is, random, spatial distribution of the objects in a scene rather than implementing the spatially explicit locations prescribed on the RAMI Web site; MBRF uses rectangular leaves rather than disc-shaped ones; RGM emulates leaf shapes by aggregating small triangular primitives; and the Sprint3 model always uses statistical distributions (rather than deterministic placements) of the foliage elements. These structural deviations, which are often motivated by the need for elegant and speedy solutions to the RT equation, may, however, become relevant in an intercomparison exercise like RAMI.

[14] *Widlowski et al.* [2005] recently showed that vegetation canopies with identical domain-averaged state variable values but different structural representations will, in general, yield different multiangular BRF patterns. In the context of RAMI, one may thus expect differences to occur between RT models featuring exact representations of the prescribed canopy structures and (1) improved/expanded versions of essentially plane-parallel RT models in simulations over structurally heterogeneous canopy targets or (2) RT models that rely implicitly on 3-D plant structures (i.e., Geometric Optical models) when applied to structurally homogeneous test cases. For these reasons the MAC (4SAIL2) model, which utilizes a parameterized formalism to distribute vegetation elements (gaps) within each elevation of its (one or two layer) vegetation canopy representation, may deviate from the RT quantities simulated using models that make use of the actual location of vegetation elements in the heterogeneous RAMI test cases. Similarly, the simulations of the 5Scale model in the context of 1-D canopies have not been included in this manuscript.

[15] In order to obtain a comprehensive indication of the performance of a RT model in forward mode, it is essential to run it on as large an ensemble of structurally and spectrally different canopy scenarios as possible, without, however, compromising the structural premises on which its internal canopy representation is based. Thus the greater the degree of realism and the larger the structural diversity of the available number of RAMI test cases is, the more indicative the observed BRF deviations between the various RT models and/or some "surrogate truth" will become. Last but not least, one should also note that the performance of many 1-D and 3-D RT models could always be improved through the usage of more precise numerical integration schemes, as well as larger numbers of ray trajectories in the case of some of the MC models. Such a "tuning" of model performances would, however, be of little interest to model users if (1) the publicly available versions of these computer codes cannot deliver these accuracies and (2) the computation times to achieve such accuracies become prohibitive in the daily usage of the models.

[16] When constrained to evaluate model simulations in the absence of any absolute reference standard or "truth," as is the case with RAMI, *Pinty et al.* [2001] argued that RT model benchmarking on the basis of statistical moments, derived from the entirety of participating models, may be biased in the presence of outliers. Instead they proposed a relative evaluation scheme where the simulations of individual models are compared against those from all other participating models over as large as possible a set of conditions. In this way, RT models that are consistently different from others can be identified [*Pinty et al.*, 2004b]. The same authors also note that internal inconsistencies in one or more submodules of a given RT model may compensate each other and lead to apparently correct overall BRF estimates. They thus recommend the evaluation of BRF components as well as the total BRFs generated by a model. In the following, the three-step invalidation procedure from section 2 will be applied to both the homogeneous and heterogeneous baseline scenarios of RAMI-3. More specifically, subsection 3.1 will investigate the internal self-consistency of the models that participated in the baseline scenarios of RAMI-3. Subsection 3.2 then looks at RT model performance in situations where exact analytical solutions are available. Finally, subsection 3.3 documents various aspects of relative model intercomparison with respect to the discrete homogeneous and the "floating spheres" baseline scenarios.

3.1. Model Self-Consistency

[17] It is difficult to offer meaningful interpretations as to why the output of a given RT model may be different from simulation results of other models without verification of the models' internal consistency. Energy conservation, for example, is one of the key principles to ensure, and this both with respect to directional (BRFs) and hemispherically integrated (fluxes) quantities.

3.1.1. Energy Conservation

[18] The solar radiation entering a plant canopy is partitioned into an absorbed A, a reflected R and a transmitted T fraction such that all incident photons are accounted for. Energy conservation thus requires that $A + R + (1 - \alpha)T = 1$, where α is the soil brightness. The capacity of a given model (m) to conserve energy can be described using:

$$\Delta_F(m) = \frac{1}{N_F(m)} \sum_{\lambda=1}^{N_\lambda^m} \sum_{\zeta=1}^{N_\zeta^m} \sum_{i=1}^{N_{\Omega_i}^m} [A_m(\lambda,\zeta,i) + R_m(\lambda,\zeta,i) + [1-\alpha(\lambda)]\, T_m(\lambda,\zeta,i)] - 1$$

where $N_F(m) = N_\lambda^m + N_\zeta^m + N_{\Omega i}^m$ is the total number of spectral λ, structural ζ, and illumination Ω_i conditions for which flux simulations were performed by model m. Figure 2 shows the mean deviation from energy conservation, $\Delta_F(m)$ for those models that simulated flux quantities in the case of the structurally homogeneous baseline scenarios. More specifically, Figure 2 (top) displays $\Delta_F(m)$ for canopies with discrete leaves in the solar domain, and Figure 2 (bottom) shows $\Delta_F(m)$ for turbid medium canopies with conservative scattering properties (purist corner). It should be noted that the MAC model seems to generate an excess of energy ($\Delta_F(MAC) > 0$) that is equivalent to about 3% of the incident radiation at the TOC in the solar domain. On the other hand, the FLIGHT and raytran models both appear to lose energy ($\Delta_F < 0$), equivalent to $\sim$2% of the incident radiation at those wavelengths. Under conservative scattering conditions, however, the latter two models comply very well with energy conservation requirements ($\Delta_F \approx 0$), a pattern that is observed for both discrete and turbid medium foliage representations in structurally homogeneous, as well as heterogeneous environments (not shown). Since $\alpha = 1$ under purist corner conditions it must be the canopy

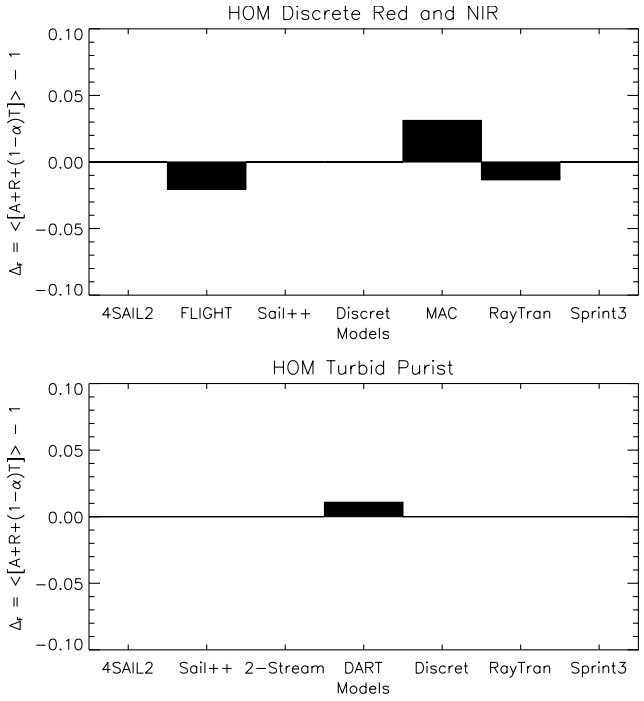

Figure 2. Average deviation from energy conservation (Δ_F) for RT models performing (top) the discrete homogeneous baseline scenarios in the solar domain and (bottom) the turbid medium homogeneous test cases under conservative scattering conditions.

transmission measurement that affects Δ_F for both FLIGHT and raytran. Indeed, in the case of raytran it turned out that the diffuse transmission component had been neglected in the submitted simulations. By the same token the deviations of the DART model under conservative scattering conditions are likely to arise from its estimation of the canopy absorption and/or reflectance. Further analysis (not shown) indicated that enhanced multiple scattering conditions exacerbate the apparent deviations from energy conservation for all models with nonzero Δ_F values in Figure 2. As to how much these apparent deviations from energy conservation relate to model deficiencies rather than operator errors is, however, difficult to anticipate. By the same token, RT models that utilize the principle of energy conservation to close their radiation budget will obviously never be found deviating in such self-consistency checks. This applies, for example, to the 1/2-discret, Sail++ and 2-Stream models which derive their canopy absorption estimate from simulations of the reflectance and transmission properties of the vegetation layer.

3.1.2. BRF Consistency

[19] The RAMI format specifications ask for all radiative quantities to be provided with a precision of six decimal places, i.e., the implicit error associated with the measurements is thus of the order of 10^{-6}. The average absolute difference $\Delta\rho$ between the total BRF (ρ_{tot}) and the sum of the BRF contributions due to the single uncollided (ρ_{uc}), the single-collided (ρ_{co}), and the multiple-collided (ρ_{mlt}) radiation components should thus be of a similar magnitude when defined as follows:

$$\Delta\rho(m) = \frac{1}{N_\rho(m)} \sum_{\lambda=1}^{N_\lambda^m} \sum_{\zeta=1}^{N_\zeta^m} \sum_{v=1}^{N_{\Omega_v}^m} \sum_{i=1}^{N_{\Omega_i}^m} \left| \rho_{tot}^m(\lambda,\zeta,v,i) - \left[\rho_{uc}^m(\lambda,\zeta,v,i) + \rho_{co}^m(\lambda,\zeta,v,i) + \rho_{mlt}^m(\lambda,\zeta,v,i)\right] \right|$$

where $N_\rho(m) = N_\lambda^m + N_\zeta^m + N_{\Omega v}^m + N_{\Omega i}^m$ is the total number of BRFs that were generated with the model m for different spectral λ, structural ζ, viewing Ω_v, and illumination Ω_i conditions. Apart from Hyemalis and 2-Stream, all models in Table 1 provided simulations of the three BRF components for at least some of the test cases of RAMI-3. In general, the average absolute deviation $\Delta\rho$ was $<10^{-5}$, with the exception of $\Delta\rho(5Scale) = 0.0027$ for the discrete homogeneous solar domain, as well as $\Delta\rho(frat) = 0.0013$ and $\Delta\rho(FLIGHT) = 0.0002$ for the homogeneous discrete purist corner. These deviations, although small in terms of the magnitude of the total BRF and often related to the configuration of the model in its day to day usage, are nevertheless significant in the context of a model intercomparison exercise like RAMI since, by their statistical nature, they seem to indicate that some of the models do not conserve energy when partitioning the total BRF into its various subcomponents.

3.1.3. Spectral Ratio of the Single-Uncollided BRF

[20] Model self-consistency can also be evaluated across different wavelengths. The ratio $\rho_{uc}(\lambda_1)/\rho_{uc}(\lambda_2)$ of the single-uncollided BRF components in the red and NIR spectral regimes, for example, relates to the differing amounts of radiation that have been scattered once by the underlying background (and never interacted with the canopy foliage) at these two wavelengths (λ_1 and λ_2). In the case of Lambertian soils, this spectral ratio must be a directionally invariant constant equal to the ratio of the soil albedos at the wavelengths of interest, i.e., $\alpha(\lambda_1)/\alpha(\lambda_2)$. Ensemble-averaging over a variety of structure ζ and illumination Ω_i conditions ($N_S = N_\zeta^m + N_{\Omega i}^m$) then provides an indication of the average deviation from spectral consistency for any model m:

$$\Delta_S(m,\Omega_v) = \frac{\alpha(\lambda_1)}{\alpha(\lambda_2)} - \left[\frac{1}{N_S(m)} \sum_{\zeta=1}^{N_\zeta^m} \sum_{i=1}^{N_{\Omega_i}^m} \frac{\rho_{uc}^m(\lambda_1,\zeta,\Omega_v,i)}{\rho_{uc}^m(\lambda_2,\zeta,\Omega_v,i)}\right]$$

Figure 3 documents the angular variation of Δ_S, obtained from single-uncollided BRF simulations in the red and NIR spectral domains, for homogeneous turbid medium (left) and discrete floating spheres canopies (right) having uniform LNDs. Not included in these graphs are the forward MC ray-tracing models frat and raytran because of the large noise levels associated with their sampling schemes. MC noise is also evident for the drat and Rayspread models, although this decreases as more rays are being used in the RT simulation and/or the fraction of the contributing background in the scene increases, e.g., in the "floating spheres" scenarios. One will notice that, with the exception of the Sprint3 model in the "floating spheres" case, the spectral ratio of the single-uncollided BRF component remains relatively constant for all models

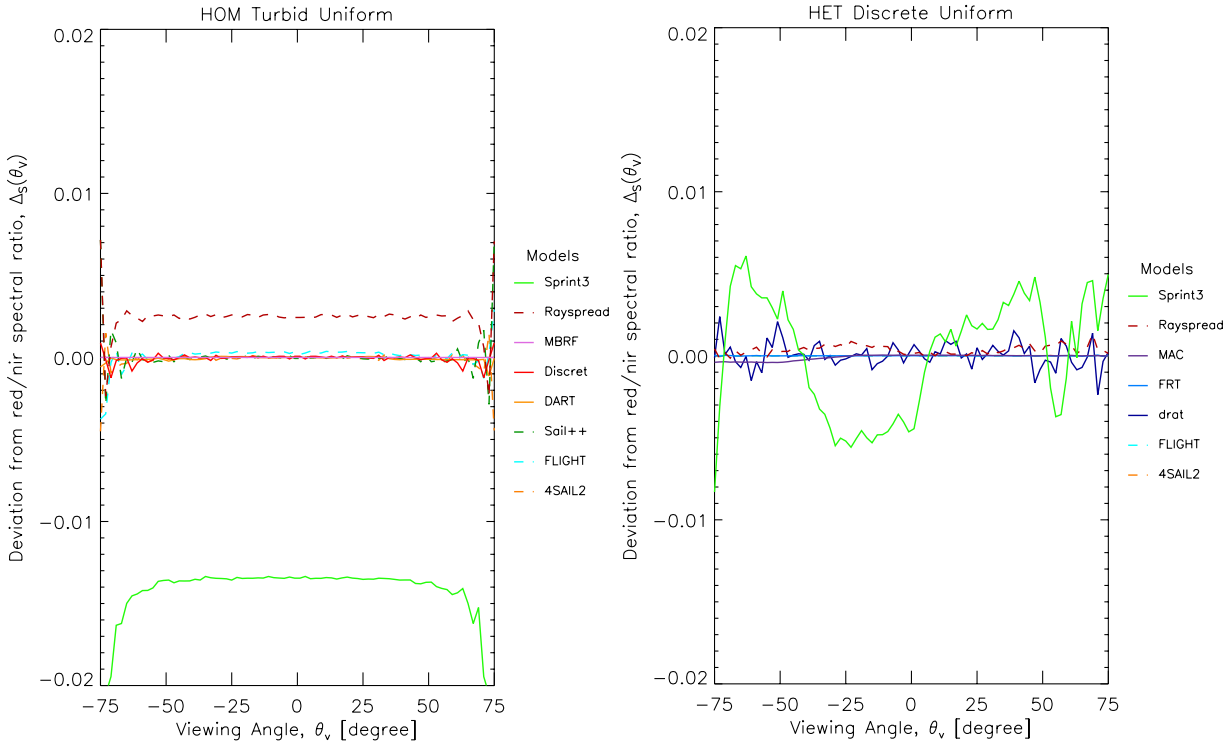

Figure 3. Average deviation from the true spectral ratio of the single-uncollided BRF components in the red and NIR spectral domains, Δ_S, as a function of view zenith angle for (left) homogeneous turbid medium canopies and (right) discrete floating spheres canopies with uniform LNDs.

(including ACRM in the homogeneous discrete case, not shown) up to view zenith angles of about 65–70°. The Sprint3 model, and to a lesser extent also the Rayspread model, utilize a variance reduction technique known as "photon spreading" in order to reduce the number of rays that sample the radiative transfer properties of the medium of interest. In Figure 3 the deviations in the magnitude but not in the shape of the single-uncollided BRF components in the homogeneous turbid case (Figure 3, left) may thus be solely due to an insufficient sampling (LAI = 3) of the lower boundary condition contributing to ρ_{uc}. On the other hand, the variations of Δ_S(Sprint3) with view zenith angle in the "floating spheres" case (LAI = 2.36) may be due to the spatially varying presence of foliage in the canopy together with the statistical distribution of foliage, rather than a deterministic placement of scatterers, within the various spherical volumes. As such the actual number of rays, that traverse the floating spheres (LAI = 5) and reach the ground or escape the scene unhindered, is never the same in different directions if model runs at different wavelengths do not use the same starting seeds to initialize their random number generator.

3.2. Absolute Model Performance

[21] Exact analytical solutions to the radiative transfer equation do not exist for the vast majority of conceivable vegetation canopies. In some cases, however, the structural and spectral properties of vegetated surfaces may be such that it becomes possible to predict at least some of their radiative properties analytically. Within the available set of RAMI test cases there are at least two different types of absolute model evaluations that can be performed: The first one relates to single-collided BRF components of structurally homogeneous turbid medium canopies with uniform LND, and the second to the reflected and absorbed energy fluxes in the various conservative scattering (purist corner) scenarios.

3.2.1. Homogeneous Turbid Uniform Canopy

[22] Structurally homogeneous leaf canopies with azimuthally invariant uniform LNDs are characterized by a constant probability of foliage interception irrespective of the direction of propagation in that medium [*Ross*, 1981; *Verstraete*, 1987]. In addition, turbid media, with their infinitesimally small scatterers, satisfy the far field approximation and thus never yield a hot spot, i.e., a localized increase in the BRF around the retroreflection direction of the incident illumination, e.g., [*Gerstl*, 1988; *Verstraete*, 1988; *Kuusk*, 1991]. The single-uncollided BRF component of such a canopy can be written as:

$$\rho_{uc}(\Omega_i, \Omega_v) = \alpha \exp\left[\frac{-\mathrm{LAI}(\mu_i + \mu_v)}{2\mu_i\mu_v}\right]$$

where α is the albedo of the Lambertian soil, $\mu = \cos\theta$ is the cosine of the illumination (i) or view (v) zenith angle $0 \leq \theta \leq \pi/2$, and LAI is the leaf area index of the canopy. Similarly the single-collided BRF component of such a canopy can be written as:

$$\rho_{co}(\Omega_i, \Omega_v) = \frac{2\Gamma(\Omega_i \rightarrow \Omega_v)\left[1 - \exp\dfrac{-\mathrm{LAI}(\mu_i + \mu_v)}{2\mu_i\mu_v}\right]}{\mu_i + \mu_v}$$

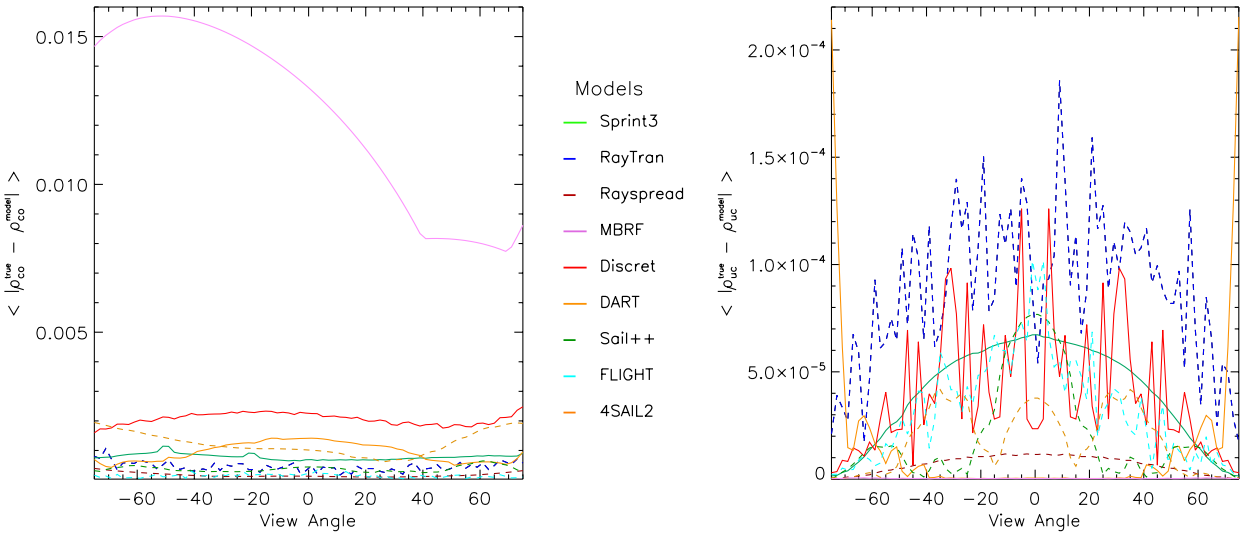

Figure 4. Mean absolute error between model simulations and the analytical formulation of (left) the single-collided, ρ_{co}, and (right) the single-uncollided, ρ_{uc}, BRF components of a homogeneous turbid medium canopy with uniform LND and Lambertian scattering laws. For any view zenith angle the averaging was performed over the principal and orthogonal plane, as well as for illumination zenith angles of 20° and 50°.

where the canopy scattering phase function is given by [*Shultis and Myneni*, 1988]:

$$\Gamma(\Omega_i \rightarrow \Omega_v) = \frac{r_L + t_L}{3\pi}(\sin\beta - \beta\cos\beta) + \frac{t_L}{3}\cos\beta$$

and β is the phase angle between the illumination and viewing direction:

$$\cos\beta = \cos\theta_i \cos\theta_v + \sin\theta_i \sin\theta_v \cos|\phi_i - \phi_v|$$

and r_L (t_L) is the reflectance (transmittance) of the foliage elements. Figure 4 shows the mean absolute error between RT model simulations and the above analytical formulations for the single-collided (Figure 4, left) and the single-uncollided (Figure 4, right) BRF components of a turbid medium canopy with uniform LND and Lambertian scattering laws. The averaging was performed over BRF simulations in the principal and orthogonal planes, as well as for illumination zenith angles of 20° and 50°. With the exception of MBRF all RT models lie within 0.0025 of the truth in the single-collided case. The operator of the MBRF model conjectures, however, that the observed deviations may be due to a software error (bug) since the formulation of the single-collided BRF component in the work by *Qin and Xiang* [1997] is based on a proper theoretical derivation. In the single-uncollided case the agreement between the participating RT models and the analytical solution is ten times better still than in the single-collided case, i.e., all models lie within 2.5 10^{-4} of the analytical solutions. This is impressive since the magnitude of ρ_{co} (ρ_{uc}) along the orthogonal plane was typically around 0.017 (0.003) in the red and 0.16 (0.005) in the NIR. Furthermore, it should be noted that none of the participants had any a priori knowledge about these absolute evaluation tests. In principle, the performance of many of the participating RT models could thus still be improved further, for example, by increasing the number of integration steps (e.g., Gaussian quadrature points) in numerical techniques, or, by adding further rays to sample the characteristics of the canopy-leaving radiation field (in the case of MC ray-tracing models).

3.2.2. Purist Corner Fluxes

[23] Under conservative scattering conditions all of the energy that enters a canopy system has to leave it, i.e., $R = 1$ and $A = 0$. The RAMI purist corner thus provides another opportunity to assess the performance of RT models against a known absolute reference. Figure 5 shows (on a log-log scale) the average absolute deviation ε from the true canopy absorption (y axis) and reflectance (x axis) for homogeneous canopies with finite-sized (Figure 5, left), as well as turbid medium (Figure 5, right) foliage representations under conservative scattering properties. In each case the averaging was performed over (N = 18) test cases with different LAI, LND and θ_i. With the exception of MBRF, which did not provide absorption estimates, all models featuring $\varepsilon = 10^{-7}$ (or -7 in Figure 5) submitted the theoretical values. In the homogeneous turbid case, for example, both the raytran, and Sprint3 models compute the canopy absorption and reflectance to within computer-precision uncertainties. The 1/2-discret and 2-Stream models, on the other hand, showed an average absolute deviation of 0.0015 and 0.0245, respectively, for both $\varepsilon_{\text{Absorption}}$ and $\varepsilon_{\text{Reflectance}}$. Models that fall on the 1:1 line in Figure 5 estimate their canopy absorption by closing the energy budget. In the case of the 1/2-discret model the (negative) canopy absorption deviations arose from overestimated albedos under the fully scattering purist corner conditions. These in turn, are a consequence of the fixed number (16) of Gaussian quadrature points used in the numerical integration scheme of the

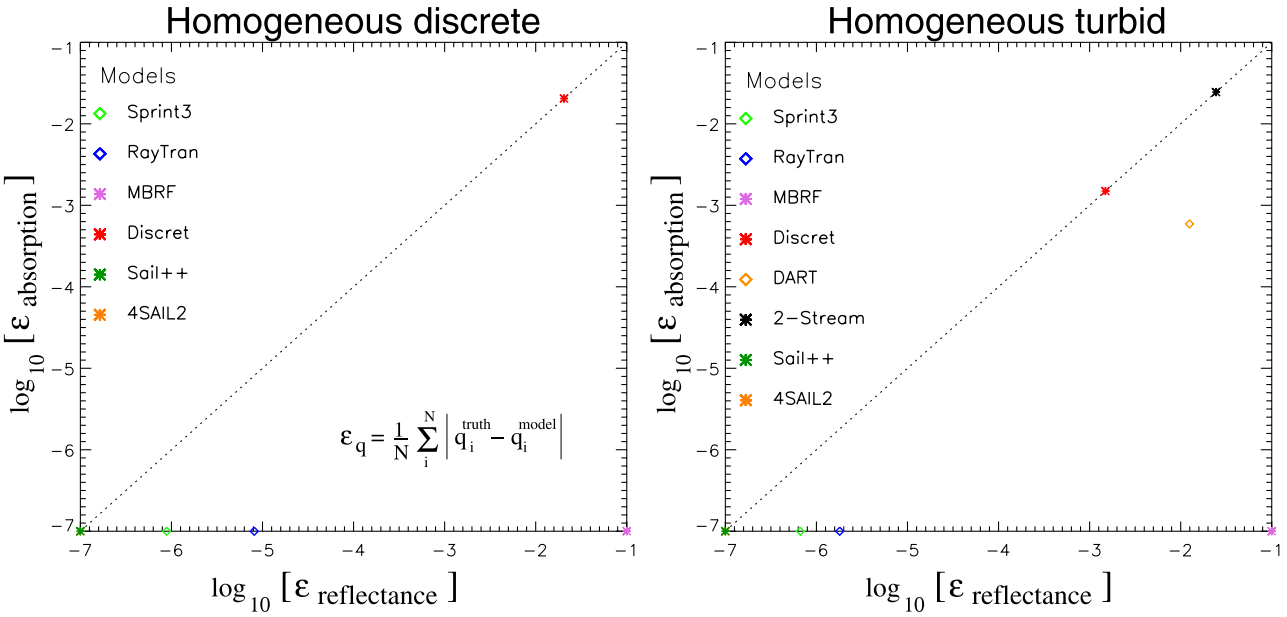

Figure 5. Average absolute deviation, ε_q, between RT model estimates and the true canopy absorption, $q^{\text{truth}} = A = 0$ (y axis) or reflectance $q^{\text{truth}} = R = 1$ (x axis), on a logarithmic scale, for structurally homogeneous canopies with (left) finite-sized and (right) turbid medium foliage representations under conservative scattering conditions. The averaging was performed over N = 18 test cases with varying LAI, LND and θ_i. Note that, with the exception of MBRF which did not provide absorption estimates, all exact A and R values are plotted at log $\varepsilon_q = -7$.

azimuthally averaged multiple-scattering component. The DART model, on the other hand, which computes canopy absorption on a ray-by-ray basis, features a respectable $\varepsilon_{\text{Absorption}} = 0.0006$ and $\varepsilon_{\text{Reflectance}} = 0.0125$. In the discrete homogeneous case (Figure 5, right), the average absolute deviation of the 1/2-discret model from the correct absorption and reflectance values increases to 0.0204, presumably because of highly variable BRFs in the vicinity of the retroreflection direction (hot spot) that affected the accuracy of the numerical integration scheme. At this point, one should recall that the lack of deviations from the "truth" is not a proof of the physical correctness of a model since, for example, hard-encoded programming statements may be contained inside the computer code that do account for the eventuality of situations for which the exact solution is known. In this way, the actual model would not be executed, to compute canopy reflectance and absorption here, but sidestepped to generate the anticipated results. The primary interest here (and in all other parts of section 3) thus lies in understanding the observed deviations from the correct solution.

3.3. Relative Model Performance

[24] Without access to absolute reference standards the evaluation of RT models has to rely on relative model intercomparison. The goal being to identify systematic trends in the behavior of one (or more) models with respect to others, over ensembles of test cases. Three different types of relative intercomparison metrics will be proposed here: model-to-model deviations, model-to-ensemble deviations, and deviations from model-derived surrogate truths.

3.3.1. Model-to-Model Deviations

[25] The differences in the BRF simulations between two models (c and m), when averaged over a variety of spectral (λ), structural (ζ), viewing (Ω_v) and illumination (Ω_i) conditions, can be defined as:

$$\delta_{m\leftrightarrow c} = \frac{200}{N}\sum_{\lambda=1}^{N_\lambda}\sum_{\zeta=1}^{N_\zeta}\sum_{v=1}^{N_{\Omega_v}}\sum_{i=1}^{N_{\Omega_i}}\left|\frac{\rho_m(\lambda,\zeta,v,i)-\rho_c(\lambda,\zeta,v,i)}{\rho_m(\lambda,\zeta,v,i)+\rho_c(\lambda,\zeta,v,i)}\right|$$

where $N = N_\lambda + N_\zeta + N_{\Omega v} + N_{\Omega i}$ is the total number of BRF simulations that have been performed by both models c and m, and $\delta_{m\leftrightarrow c}$ is expressed in percent.

[26] Figure 6 depicts a series of two-dimensional grids containing information on the various model-to-model BRF differences (blue-red color scheme in the lower right half of each panel), as well as the percentage of the total number of BRFs over which the $\delta_{m\leftrightarrow c}$ values were derived (black-green color scheme in upper left half of each panel). More specifically, $\delta_{m\leftrightarrow c}$ is shown for those models having submitted the total (first row), single-uncollided (second row), single-collided (third row) and multiple-collided (fourth row) BRF data for structurally homogeneous canopies with finite-sized (first column) and turbid medium (second column) foliage representations, as well as for "floating spheres" scenarios with finite-sized (third column) and turbid medium (fourth column) foliage representations in the solar domain. The blue color scale increments in steps of 2%, the green color scale in steps of 10%, and the red also in steps of 10% with the bright red color indicating values larger than 50%. The maximum number of BRF simulations

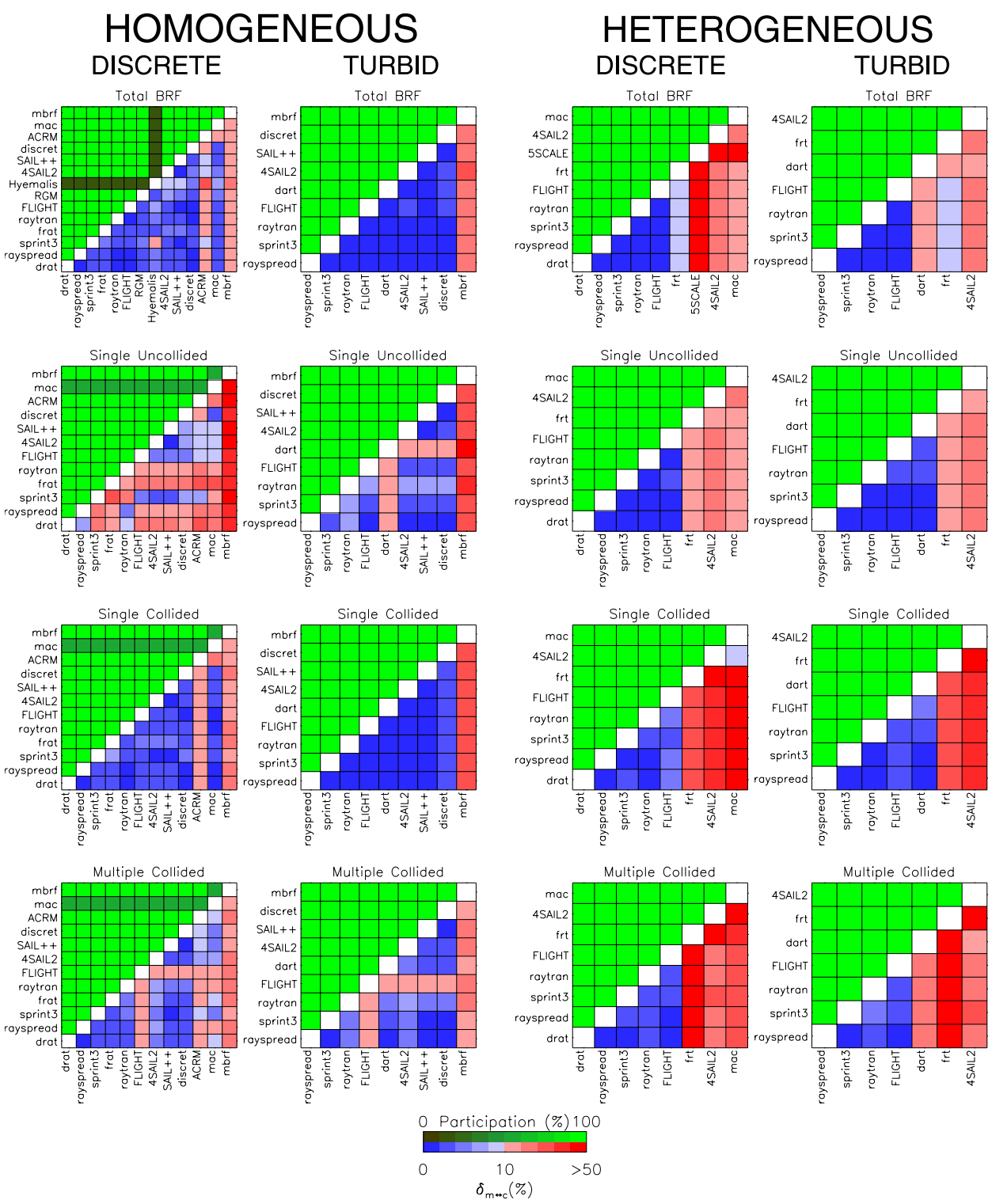

Figure 6. Model-to-model differences $\delta_{m\leftrightarrow c}$ of the total (first row), single-uncollided (second row), single-collided (third row), and multiple-collided (fourth row) BRF data of models performing the required simulations for structurally homogeneous canopies with finite-sized (first column) and turbid medium (second column) foliage representations, as well as for "floating spheres" scenarios with finite-sized (third column) and turbid medium (fourth column) foliage representations in the solar domain. The lower right half of every panel indicates $\delta_{m\leftrightarrow c}$ in [%] (blue-red color scheme), whereas the top left half indicates the percentage of available test cases that pairs of models performed together (black-green color scheme). The green color scale increments in steps of 10%, the blue color scale increments in steps of 2% (up to $\delta_{m\leftrightarrow c} = 10\%$), and the red color scale increments in steps of 10% (with a bright red color indicating $\delta_{m\leftrightarrow c} > 50\%$).

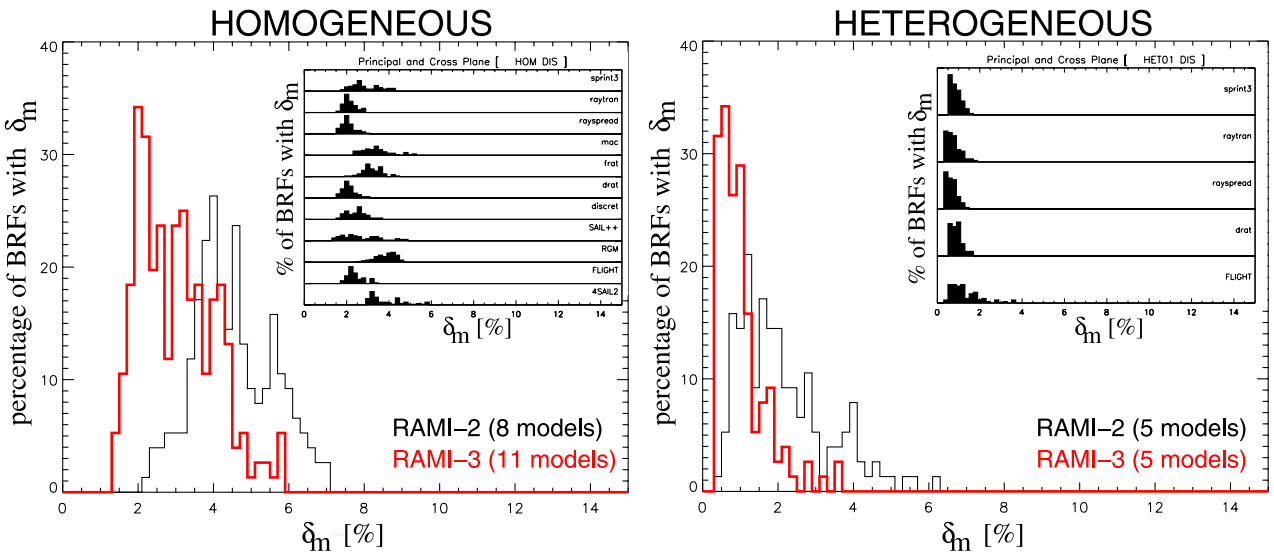

Figure 7. The insets show histograms of model-to-ensemble differences, δ_m [%] for selected models participating in the (left) discrete homogeneous and (right) discrete "floating spheres" test cases. Included in the generation of these histograms are BRF simulations in the principal and orthogonal planes using illumination zenith angles of 20° and 50° in both the red and NIR spectral domain. The main panels show the envelope encompassing the various RAMI-3 (red color) histograms, shown in the insets, in relation to that obtained during RAMI-2 (black line) for the same set of test cases.

included in the computation of $\delta_{m\leftrightarrow c}$ was 1216 for the structurally homogeneous and 608 for the "floating spheres" canopies. To illustrate the reading of the various panels in Figure 6 let us consider, for example, the total BRFs of the Hyemalis and Sprint3 models in the discrete homogeneous case (Figure 6, top left): Their model-to-model difference value, which lies between 10 and 20% (light red color), has been obtained from less than 10% of the total number of BRF simulations (dark green color) and thus may not be too representative. On the other hand, the $\delta_{m\leftrightarrow c}$ of the ACRM and Sprint3 models (Figure 6, top left) lies somewhere between 6 and 8% and has been established using 100% of the possible BRFs. In general, the majority of models in the discrete and turbid homogeneous cases agree rather well with each other ($\delta_{m\leftrightarrow c} < 10\%$). This behavior is also present for the various BRF components with the exception of the single-uncollided BRF component (ρ_{uc}) in the discrete homogeneous case where the various implementations/approximations of the hot spot phenomenon have increased the differences amid the simulated BRFs. In the case of turbid homogeneous canopies the DART model features somewhat elevated $\delta_{m\leftrightarrow c}$ values for the ρ_{uc} component which may, however, be partly due to the inter/extrapolation procedure that had to be systematically applied to all BRF simulations of this model in order to map its submitted 32 (18) viewing conditions in the principal (orthogonal) plane to the full set of 76 as specified by RAMI. The FLIGHT model, which did not update its baseline scenario simulations during RAMI-3, shows slightly diverging multiple-collided BRF components in both the discrete and turbid medium homogeneous cases. These are caused by a Lambertian assumption governing the angular distribution of higher orders of scattered radiation in simulation results originally submitted during RAMI-1. This effect is no longer visible in the "floating spheres" case because of subsequent model improvements in phase 2 (Figure 6, right). Unlike in the discrete homogeneous cases, the "floating spheres" ρ_{uc} shows the smallest $\delta_{m\leftrightarrow c}$ values presumably because the hot spot signature here is dominated by the geometry of the spheres themselves. In the "floating spheres" cases it is thus the multiple scattering and to a lesser extent also the single-collided BRF components that show the largest differences between BRF simulations of 3-D Monte Carlo models, featuring explicit scene representations, and those of somewhat more approximate models.

3.3.2. Model-to-Ensemble Deviations

[27] In the absence of any absolute reference truth, the output from individual RT models may also be compared to ensemble averages computed from simulation results of other RT models, as first proposed by *Pinty et al.* [2001, 2004b]. In this way, RT models that are very different from all other models can be identified and, although not wrong in any absolute sense, they may then be excluded from further iterations of the ensemble averaging process, if this is deemed appropriate. For any spectral (λ), structural (ζ), viewing (v), and illumination (i) condition one can compute:

$$\delta_m(\lambda,\zeta,v,i) = \frac{200}{N_c}\sum_{c=1;c\neq m}^{N_c}\left|\frac{\rho_m(\lambda,\zeta,v,i)-\rho_c(\lambda,\zeta,v,i)}{\rho_m(\lambda,\zeta,v,i)+\rho_c(\lambda,\zeta,v,i)}\right|$$

where N_c is the number of models with which the output of model m is to be compared. One way to analyze such δ_m statistics is to bin them over a variety of conditions in order to yield a histogram of model-to-ensemble deviations. The insets in Figure 7 show a variety of δ_m histograms generated from total BRF simulations of the 1/2-discret, drat,

Table 2. Model-to-Ensemble Dispersion Statistics, $\bar{\delta}_m$ for Six 3-D Monte Carlo Models in RAMI-2 and RAMI-3[a]

		Discrete Scenes		Turbid Scenes	
Model Name	BRF Type	RAMI-2	RAMI-3	RAMI-2	RAMI-3
DART	ρ_{tot}	-	-	1.42	1.46
DART	ρ_{co}	-	-	1.80	0.81
DART	ρ_{mlt}	-	-	21.44	2.72
DART	ρ_{uc}	-	-	29.02	2.40
drat	ρ_{tot}	1.92	0.55	-	-
drat	ρ_{co}	15.98	1.43	-	-
drat	ρ_{mlt}	3.49	1.14	-	-
drat	ρ_{uc}	72.93	7.47	-	-
FLIGHT	ρ_{tot}	1.26	0.97	9.63	1.06
FLIGHT	ρ_{co}	19.92	3.08	12.72	1.66
FLIGHT	ρ_{mlt}	3.33	2.79	15.40	3.10
FLIGHT	ρ_{uc}	32.99	10.80	14.29	4.48
Rayspread	ρ_{tot}	-	0.55	-	0.64
Rayspread	ρ_{co}	-	1.42	-	0.69
Rayspread	ρ_{mlt}	-	1.18	-	1.48
Rayspread	ρ_{uc}	-	5.88	-	2.62
raytran	ρ_{tot}	1.31	0.60	1.06	0.69
raytran	ρ_{co}	10.24	1.38	1.47	0.78
raytran	ρ_{mlt}	2.73	1.32	10.29	1.81
raytran	ρ_{uc}	32.62	7.20	12.83	3.61
Sprint3	ρ_{tot}	1.29	1.01	9.66	0.69
Sprint3	ρ_{co}	9.11	2.12	12.67	0.94
Sprint3	ρ_{mlt}	2.44	1.61	15.27	1.61
Sprint3	ρ_{uc}	31.53	7.94	15.72	3.44

[a]In each case, the averaging was performed over all available structural, spectral, illumination and viewing conditions. Unit is percent.

FLIGHT, frat, Rayspread, raytran, RGM, Sail++, Sprint3, and 4SAIL2 models in the case of the discrete structurally homogeneous canopies (Figure 7, left), and the drat, FLIGHT, Rayspread, raytran, and Sprint3 models in the case of the discrete ''floating spheres'' canopies (Figure 7, right). The main graphs of Figure 7 show the outer envelope of these δ_m histograms both for the discrete structurally homogeneous canopies (Figure 7, left) and the discrete ''floating spheres'' canopies (Figure 7, right). One will notice that the agreement between the RT models in RAMI-3 (red line) is better than the corresponding agreement of models during the previous phase of RAMI three years ago (black line). In the homogeneous baseline scenarios, where more models are included than during RAMI-2, the first peak of the histogram envelope ($0 \leq \delta_m \leq 2.5\%$) can be attributed primarily to the models 1/2-discret, drat, FLIGHT, Rayspread and raytran. The second half of the histogram envelope ($\delta_m > 2.5\%$), on the other hand, arises from BRF simulations due to the models frat, MAC, RGM. The models Sail++ and Sprint3, with their broader distributions of δ_m, contribute to both parts of the histogram envelope.

[28] Alternatively one may define an overall indicator of model-to-ensemble differences, $\bar{\delta}_m$ [%] by averaging the above $\delta_m(\lambda, \zeta, v, i)$ over appropriate sets ($\bar{N}$) of spectral λ, structural ζ, viewing v and illumination i conditions:

$$\bar{\delta}_m = \frac{1}{\bar{N}} \sum_{\lambda=1}^{N_\lambda} \sum_{\zeta=1}^{N_\zeta} \sum_{v=1}^{N_{\Omega_v}} \sum_{i=1}^{N_{\Omega_i}} \delta_m(\lambda, \zeta, v, i)$$

Table 2 shows the values of the overall model dispersion indicator $\bar{\delta}_m$ [%] obtained from an ensemble of six 3-D Monte Carlo models, namely, DART, drat, FLIGHT, Rayspread, raytran and Sprint3. For each one of these models $\bar{\delta}_m$ is provided for the total BRF (ρ_{tot}) as well as the single-collided (ρ_{co}), the multiple-collided (ρ_{mlt}), and the single-uncollided (ρ_{uc}) BRF components using submitted simulation results from either RAMI-2 or RAMI-3. With the exception of the total BRF simulations of DART all other $\bar{\delta}_m$ values improved between RAMI-2 and RAMI-3, meaning that a smaller dispersion exists between the BRF values of the latest version of these models. The average dispersion between the total BRF simulations of the six 3-D MC models was found to have almost halved from RAMI-2 (1.37%) to RAMI-3 (0.72%) in the discrete case, and in the turbid medium case it improved by a factor of $\sim$7 from RAMI-2 (6.36%) to RAMI-3 (0.91%).

3.3.3. Model-to-Surrogate-Truth Deviations

[29] Monte Carlo RT models allow for explicit 3-D representations of complex canopy architectures by describing these environments with (sometimes Boolean combinations of) sufficiently small geometric building blocks of known radiative properties. Solving the radiative transfer equation for such 3-D environments is then achieved through a stochastic sampling of the surface-leaving radiation field [*Disney et al.*, 2000]. Since this is a time consuming undertaking, in particular for complex 3-D scenes, the current generation of 3-D MC models differ primarily in the amount of deterministic detail that is used when constructing a scene, and, in the approach and extent to which ray trajectories are sampled within the 3-D media. Both Figure 6 and Table 2 indicate that the 3-D Monte Carlo models, DART, drat, FLIGHT, Rayspread, raytran and Sprint3 are generally in very close agreement with each other. In particular the numbers in Table 2 support their usage in attempts to provide a ''surrogate truth'' estimate against which further RT model comparisons may then be carried out. One simple way to obtain a ''surrogate truth'' estimate is by averaging the BRFs obtained from a set of $N_{3D}^{credible}$ credible 3-D MC models, that is:

$$\bar{\rho}_{3D}(\lambda, \zeta, v, i) = \frac{1}{N_{3D}^{credible}} \sum_{n=1}^{N_{3D}^{credible}} \rho_{3D}(\lambda, \zeta, v, i; n)$$

where the precise number and names of the 3-D MC models that feature within $N_{3D}^{credible}$ is selected from among the following models: DART, drat, FLIGHT, Rayspread, raytran and Sprint3. The selection procedure is applied to every RAMI experiment and measurement type individually and adheres to the following list of criteria: (1) For every RAMI BRF (flux) measurement, identify at least two (one) 3-D Monte Carlo models that do not belong to the same RT modeling school/family; (2) if two models from the same RT modeling school/family are available, e.g., Rayspread and raytran, choose the one with the least amount of apparent MC noise; (3) remove all those 3-D Monte Carlo models from the reference set that are noticeably different from the main cluster of 3-D MC simulations; (4) if sufficient models are contained in the main cluster of 3-D MC simulations then remove those models that would introduce noticeable levels of ''MC noise'' into the reference set; and (5) if there are two distinct clusters of 3-D Monte Carlo models, or, no obvious cluster at all, then use all available 3-D RT models to define a reference solution.

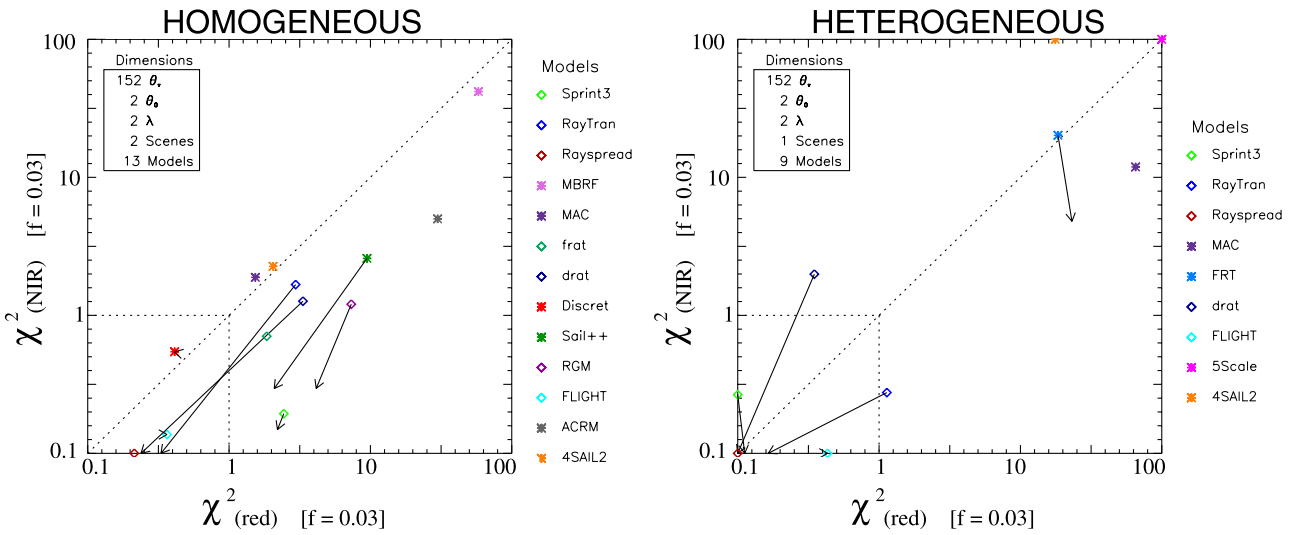

Figure 8. χ^2 statistics in the red (x axis) and NIR (y axis) wavelengths for (left) the structurally homogeneous and (right) the "floating spheres" baseline scenarios with finite sized scatterers. Arrows indicate changes in the χ^2 values of models performing both in RAMI-2 (base of arrow) and in RAMI-3 (tip of arrow) using the latter $\bar{\rho}_{3D}$ as reference.

[30] A synoptic table featuring the names of the various 3-D MC models that contribute toward the computation of $\bar{\rho}_{3D}$ for all the RAMI-3 experiments and measurement types individually, can be found on the following internet page: http://romc.jrc.it/WWW/PAGES/ROMC_Home/RAMIREF.php. Note that because of a renaming of all European Commission Web sites this URL is likely to change in the near future to http://rami-benchmark.jrc.ec.europa.eu/.

[31] Once the "surrogate truth" is available for the various RAMI baseline scenarios, the deviations of individual RT models from this norm may be quantified with the following metric [*Pinty et al.*, 2004b]:

$$\chi^2_m(\lambda) = \frac{1}{N-1} \sum_{\zeta=1}^{N_\zeta} \sum_{v=1}^{N_{\theta_v}} \sum_{i=1}^{N_{\theta_i}} \frac{[\rho_m(\lambda,\zeta,v,i) - \bar{\rho}_{3D}(\lambda,\zeta,v,i)]^2}{\sigma^2(\lambda,\zeta,v,i)}$$

where $\sigma(\lambda, \zeta, v, i) = f \cdot \bar{\rho}_{3D}(\lambda, \zeta, v, i)$ corresponds to a fraction f of the average BRF obtained from the credible 3-D Monte Carlo models.

[32] Figure 8 displays the χ^2 values in the red and NIR wavelengths for the structurally homogeneous (Figure 8, left) and the "floating spheres" (Figure 8, right) baseline scenarios having finite-sized scatterers. Arrows indicate changes in the χ^2 values when comparing the performance of a model in RAMI-2 (base of arrow) with that in RAMI-3 (tip of arrow) using the latter $\bar{\rho}_{3D}$ as reference. The uncertainty in both the model and surrogate truth was set to 3% of the latter, i.e., $f = 0.03$. This estimate is in line with the absolute calibration accuracy of current space borne instruments like MISR [*Bruegge et al.*, 2002] and MERIS [*Kneubühler et al.*, 2002], among others. Obviously there is a tendency for those 3-D MC models that have participated in the computation of $\bar{\rho}_{3D}$ to have smaller χ^2 values in RAMI-3 than in RAMI-2. This is particularly so for the heterogeneous BRF simulations, where drat, FLIGHT, Rayspread and sprint-3 served as credible models for all the "floating spheres" test cases. In the homogeneous case, however, both the number and names of the credible 3-D MC models changed from one test case to another. RT models that did not update their BRF simulations in any significant manner during RAMI-3, e.g., 1/2-discret and FLIGHT, do not show any dynamics in their χ^2 values in the depicted graphs. Others, like the Sail++ and RGM models in the homogeneous case, for example, have reduced the distance between their BRF simulations and $\bar{\rho}_{3D}$ in RAMI-3 which translates into smaller χ^2(red) and χ^2(NIR) values when compared to those of RAMI-2. FRT was the only non Monte Carlo model to participate in the "floating spheres" test cases during both RAMI-2 and RAMI-3. Here one notices a substantial improvement in its χ^2(NIR) value together with a slight increase in χ^2(red).

4. New Test Cases in RAMI-3

[33] A series of additional experiments and measurements were proposed for RAMI-3 that address new issues or complement others raised during RAMI-2. In the following, the results obtained for the "birch stand" canopy will be presented first. Next the "true zoom-in" scene, with its additional measurements, will be revisited before comparing the BRF simulation results for the "conifer forest" scene with and without topography. Last but not least, results for the "floating spheres" purist corner will also be displayed.

4.1. Birch Stand

[34] This set of experiments was suggested to simulate the radiative transfer regime in the red and near-infrared spectral bands for spatially heterogeneous scenes resembling boreal birch stands (see Figure 9). The 100 × 100 m^2 scene is composed of a large number of nonoverlapping tree-like entities of different sizes and spectral properties that are randomly located across (and only partially covering) a planar surface representing the underlying back-

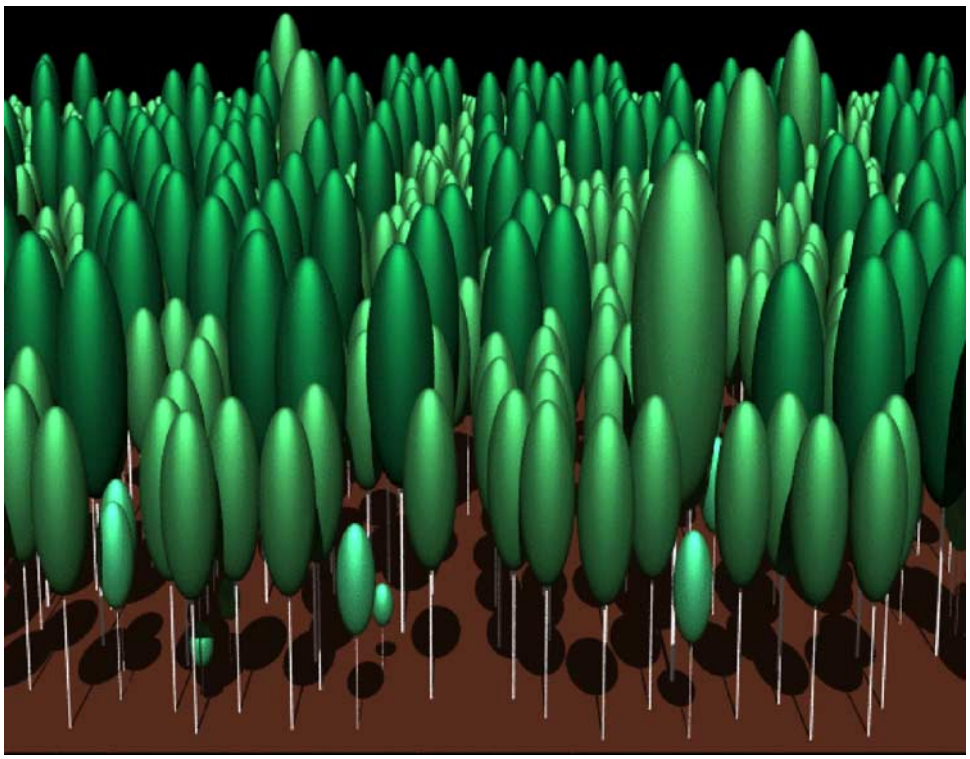

Figure 9. Graphical representation of a portion of the RAMI-3 "birch stand" scene when looking from its southern edge in an northward direction toward the center of the scene. The Sun is assumed to be located behind the viewer, i.e., "south" of the scene.

ground. Individual tree objects were represented by an ellipsoidal crown located just above a cylindrical trunk. The finite sized foliage was randomly distributed within the ellipsoidal volumes that represented the tree crowns, and was characterized by radiative properties (reflectance, transmittance) that are typical for birch trees. Table 3 provides an overview of the structural and spectral properties associated with the 5 tree classes of the "birch stand" scene.

4.1.1. Canopy-Level BRF Simulations

[35] Figure 10 presents model generated total BRFs in the red (left column) and NIR (right column) spectral domain corresponding to observations of the "birch stand" along the principal (Figure 10, top) and orthogonal (Figure 10, bottom) planes for illumination conditions of $\theta_i = 20°$ and $\theta_i = 50°$. It can be seen that most models generate relatively similar BRF patterns with the exception of 5Scale. This systematic difference may be partly explained by the fact that 5Scale implemented a "birch stand" scene composed of only one single tree class having structural and spectral properties that corresponded to the average characteristics of the 5 tree classes described on the RAMI Web site. Moreover, 5Scale's multiple scattering scheme was designed for denser forests than the "birch stand" scene with a mean LAI of 0.398. The drat model generates BRFs that, in particular in the red spectral domain, have a tendency to be somewhat higher than those of Dart, Rayspread, raytran and Sprint3. Further analysis revealed that these differences arise primarily because of the single-collided foliage BRF component. One possible explanation may be found in the exact spatial arrangement of the various discrete leaf elements that make up the crown foliage in the drat simulations. The commonly used procedure of "cloning" individual tree objects when generating a larger canopy scene, may imply that small differences in the leaf orientations and positions, especially along the rim of the crown volume, translate into noticeable differences in the simulated BRF values at the level of the whole scene. These differences are, however, only detectable because of

Table 3. Major Variables Defining the Structural and Spectral Properties Associated to the 100 × 100 m^2 "Birch Stand" Scene[a]

	Tree Class				
Parameter	A	B	C	D	E
Tree height, m	2.5	5.5	8.5	11.5	14.5
LAI/tree, m^2m^{-2}	0.751	1.081	1.340	1.575	1.805
Crown height, m	1.237	2.952	4.919	7.137	9.606
Crown width, m	0.611	0.995	1.430	1.937	2.538
Trunk height, m	1.263	2.548	3.581	4.363	4.894
Trunk width, m	0.014	0.033	0.054	0.078	0.107
Tree density, stem/ha	38	507	981	261	13
Red leaf reflectance	0.10	0.09	0.08	0.07	0.06
Red leaf transmittance	0.06	0.05	0.04	0.03	0.03
Red trunk reflectance	0.32	0.31	0.30	0.29	0.28
NIR leaf reflectance	0.49	0.48	0.47	0.46	0.45
NIR leaf transmittance	0.50	0.49	0.48	0.47	0.46
NIR trunk reflectance	0.40	0.39	0.38	0.37	0.36

[a]The reflectance of the Lambertian soil was 0.127 (0.159) in the red (NIR) spectral band. The scattering properties of both leaves and trunks were Lambertian.

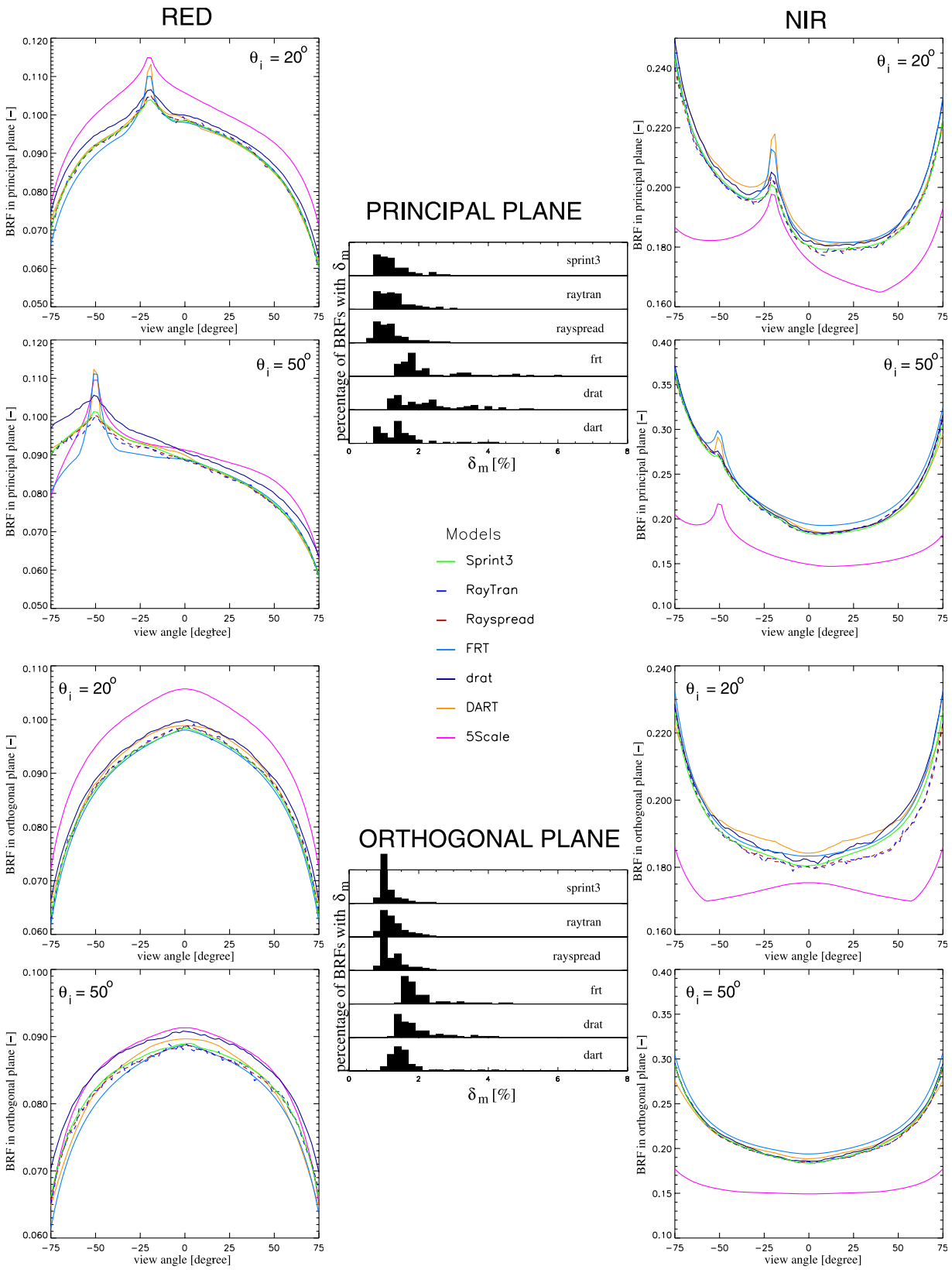

Figure 10. Model simulated BRFs in the (left) red and (right) NIR spectral domain of the "birch stand" along the (top) principal and (bottom) orthogonal planes under illumination conditions of $\theta_i = 20°$ and $\theta_i = 50°$. (middle) Histograms of model-to-ensemble deviations δ_m are provided for (all models but 5Scale in) both observational planes.

the increasing agreement that now exists between the various RT models that have contributed to RAMI-3. The histograms of model-to-ensemble BRF differences, δ_m in the "birch stand" scene (Figure 10, middle), for example, show that the BRFs simulated by any one of the models Dart, drat, frt, Rayspread, raytran and Sprint3 typically fall within 2% of the ensemble average, and this irrespective of the plane of observation.

4.1.2. Local Transmission Transects

[36] Since the x, y location of every individual tree in the "birch stand" scene was specified on the RAMI Web site a new measurement type, asking for local transmission measurements along a transect of 21 adjacent 1×1 m^2 patches, had been proposed. Models were asked to provide simulation results quantifying the total (i.e., direct plus diffuse) transmission of radiation at the level of the background for two transects located at the center of the birch stand scene with orientations that were parallel and perpendicular to the azimuthal direction of the incident radiation, ϕ_i, respectively. This setup, which aimed at reproducing conditions resembling those encountered in actual field measurements, was rather demanding on the capabilities of most RT models. The entire birch stand scene had to be illuminated but the transmission measurements were restricted to small adjacent areas in the center of the scene. This led to only two RT models contributing to this measurement type (raytran and Sprint3). Figure 11 shows their local transmission simulations for transects oriented parallel (Figure 11, left) and perpendicular (Figure 11, right) to the direction of the illumination azimuth (ϕ_i) in both the red (Figure 11, top) and NIR (Figure 11, bottom) spectral domain. Although the simulation results are somewhat different, both models capture obvious features in the spatial pattern of the local canopy transmission. The various pink arrows indicate obvious correlations with predominantly shadowed and illuminated patches occurring along the transects depicted (in a perspective-free manner) at the top or bottom of each of the four graphs. One should also note that both models occasionally simulate local transmission values that are larger than unity (i.e., they fall within the grey shaded area at the top of each graph) which is an unambiguous signature of the presence of horizontal radiation fluxes. The occurrence of $T > 1$ is somewhat more frequent in the NIR because of the larger single-scattering albedo ($\omega_L = r_L + t_L$) of the foliage there, as well as for transect orientations that are perpendicular to ϕ_i, which are the ones least affected by shadows from adjacent tree crowns.

4.2. True Zoom-in Experiment

4.2.1. Multiscale BRF Simulations

[37] The "true zoom-in" experiment was first proposed during RAMI-2 [*Pinty et al.*, 2004b, section 2] and consists of a 270×270 m^2 scene featuring a number of spherical and cylindrical volumes, having precisely defined locations, that are filled with disc-shaped scatterers having different spectral properties [*Pinty et al.*, 2004b, Table 5 and Figure 2]. The scene itself is illuminated over its entire length whilst RT simulations are to be extracted over a set of progressively smaller target areas located at the center of the scene. The spatial resolutions of these target areas are 270, 90 and 30 m, respectively. Such true zoom-ins are useful when (1) the nature of local horizontal fluxes, arising from the deterministic occurrence of gaps and shadows in and immediately around the sampling area, are to be studied/accounted for and (2) the creation of artificial "order," due to cyclic boundary conditions that reproduce the scene ad infinitum, has to be avoided. The latter may arise when RT models have to be executed on 3-D canopy representations at very high spatial resolutions since the complexity of the scene is such that spatially extensive representations cannot be generated because of computer memory limitations.

[38] Within RAMI-3 the number of local patches in the "true zoom-in" experiment was extended to nine, such that the BRF simulations at 90 (30) m spatial resolution, when averaged over all nine patches equal that of the (central) patch at the coarser 270 (90) m spatial resolution since the TOC reference level remained the same throughout the scene. The necessity for deterministic canopy representations and the complexity of the RT simulation setup was, however, such that only drat, Sprint-3, raytran and Rayspread performed all of these simulations. Figure 12 thus restricts itself to total BRF simulations in the principal (Figure 12, top) and orthogonal (Figure 12, bottom) viewing planes for the 270 m (Figure 12, left), 90 m (Figure 12, middle) and 30 m (Figure 12, right) patches located at the center of the scene (for which also simulations from DART were available). The illumination zenith angle was set to 20° and the spectral properties of the environment feature typical NIR conditions. Going from coarse to fine spatial resolutions (Figure 12, left to right) one notices that the discrepancies between the various model simulations increase both in the principal and orthogonal planes. In particular, it is the DART and the Sprint3 models that differ from the BRF simulations of drat, Rayspread and raytran. Possible reasons for these BRF differences include (1) a magnification of the impact of small structural differences in the deterministic scene setup as the spatial resolution becomes finer and/or (2) the occurrence of different patterns of shadowing/illumination due to erroneously specified illumination azimuth angles.

4.2.2. Local Horizontal Flux Measurements

[39] In the visible part of the solar spectrum the divergence of horizontal radiation in vegetation canopies is largely controlled by the occurrence of mutual shadowing between individual canopy elements and photon channeling through the gaps between them. As the canopy target becomes smaller the likelihood of nonzero horizontal radiation balances increases, resulting in local radiative regimes that are highly variable across the overall domain of the canopy [*Widlowski et al.*, 2006b]. The interpretation, spatial distribution and upscaling of in situ measurements thus could benefit from a quantitative analysis of the magnitude (and directionality) of horizontal radiation transport, not only because this may contribute toward the design of optimal sampling schemes for future field validation campaigns, but also, because it may allow the identification of site-specific spatial resolution thresholds below which the pixel-based interpretation of remotely sensed data may no longer be adequate (without explicit accounting of horizontal radiation transport). RAMI-3 therefore introduced a horizontal flux measurement for the "true zoom-in" canopy scene, where participants were asked to simulate the total flux [W] that entered and exited through the various sides of a virtual voxel (box) encompassing the canopy at different

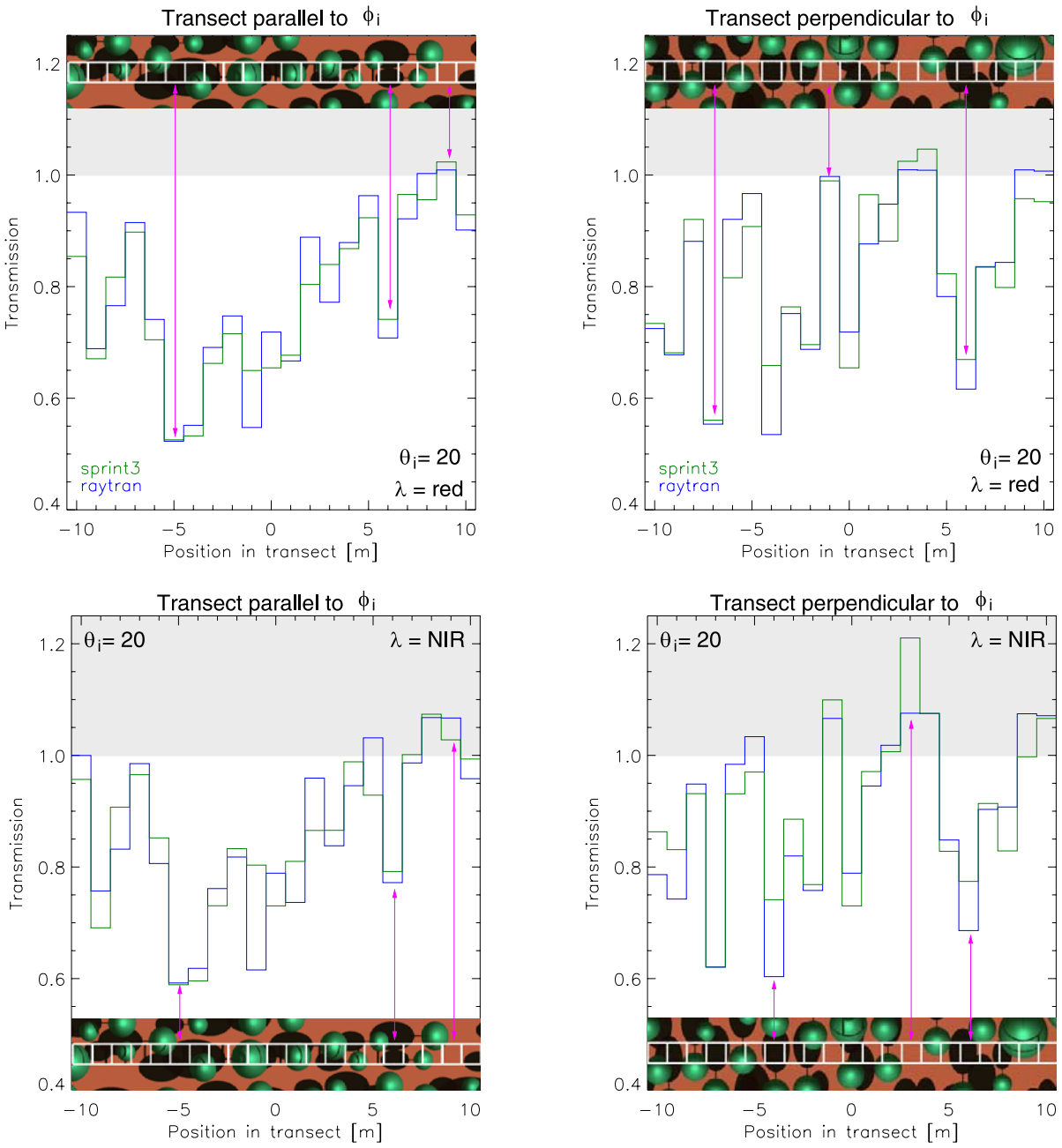

Figure 11. Model simulated local transmissions along transects composed of 21 adjacent 1 × 1 m^2 patches oriented (left) parallel and (right) perpendicular to the direction of the illumination azimuth (ϕ_i) in the (top) red and (bottom) NIR spectral domain. Pink arrows indicate obvious correlations with predominantly shadowed and illuminated patches in the various graphical representations of the transects (inlaid images featuring the transect as a sequence of white squares). Transmission values that are larger than unity fall within the grey shaded area.

spatial resolutions. These voxels, which coincide both in size and location with the local areas used for the "true zoom-in" BRF simulations, extend to a height of 15 m and have their lateral sides either parallel (constant x coordinate) or perpendicular (constant y coordinate) with the azimuth of the incident radiation, ϕ_i (see Figure 13). As was the case for the local transmission transect measurement, only a couple of models (Sprint-3 and raytran) submitted results for the local horizontal flux experiment. Figure 14 displays the results of these simulations for voxel locations corresponding to the BRF simulations depicted in Figure 12. More specifically, the various entering (solid) and exiting (dashed) total horizontal fluxes, normalized by the total incident flux at the top of the canopy, are shown for voxels with spatial dimensions equal to 270 m (left), 90 m (middle) and 30 m (right) in the NIR spectral domain. The illumination azimuth, ϕ_i is parallel (perpendicular) to the voxel sides labeled Y_{LOW} and Y_{HIGH} (X_{LOW} and X_{HIGH}), and $\theta_i = 20°$.

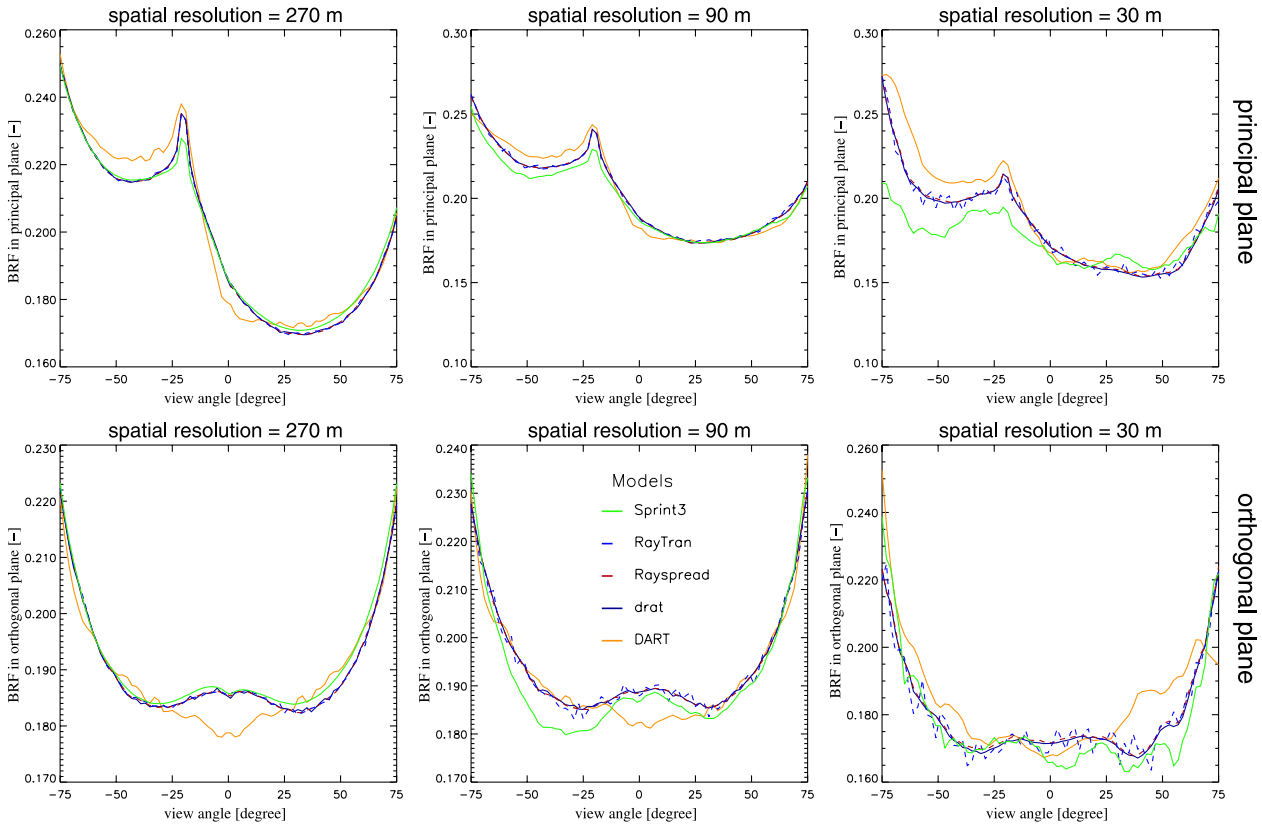

Figure 12. Model simulated BRFs along the (top) principal and (bottom) orthogonal planes of the "true zoom-in" scene at spatial resolutions of (left) 270 m, (middle) 90 m, and (right) 30 m. The illumination zenith angle was set to 20°, and the spectral properties are typical for the NIR spectral domain.

[40] The direct illumination component entering through the sunward side of a voxel (X_{HIGH}) and exiting through its opposite side (X_{LOW}) will naturally increase the magnitude of the corresponding normalized fluxes with respect to fluxes occurring in other directions and through other lateral sides of the voxel. These latter fluxes, in turn, can only arise from radiation that has been scattered by the canopy/soil system, and tend to remain directionally invariant in canopies with randomly distributed Lambertian scatterers [*Widlowski et al.*, 2006b]. By going from left to right in Figure 14, that is, from relatively large voxels to smaller ones, it can be seen that (1) the differences between entering and exiting fluxes increase, because of the increasingly nonrandom (and highly deterministic) location of shadows and gaps, and (2) the magnitude of the various horizontal fluxes increases, since the ratio of the lateral and upper voxel sides increases also. The total net horizontal flux of these voxels, i.e., the sum of all 4 laterally entering radiation streams minus the sum of the 4 laterally exiting radiation streams, when normalized by the incident total flux at the TOC level, was found to be of the order of -0.010 (-10^{-4}) at a spatial resolution of 270 m, -0.099 (-0.002) at 90 m, and 0.038 (0.007) at 30 m by the model Sprint3 (raytran). One should note that Sprint3 deviates by ~1% from the zero net horizontal radiation transport that energy conservation dictates at a spatial resolution of 270 m, since here the entire scene is contained within the voxel. The increasing magnitude of the net lateral radiation exchanges as a function of spatial resolution is, however, confirmed by both models. This behavior has to be accounted for when deriving domain-averaged canopy transmission, absorption or reflectance estimates on the basis of a series of local point measurements [e.g., *Tian et al.*, 2002; *Gobron et al.*, 2006].

4.3. Conifer Forest

[41] The "conifer forest" scene was originally proposed during RAMI-2 with the aim of simulating the radiative transfer regime in structurally heterogeneous scenes of rather large spatial extent (500 × 500 m^2) that featured tree architectures and spectral properties reflecting those of typical coniferous forests (overlying a snow background). The RAMI-2 specifications of the "conifer forest" included conical tree crown representations (of fixed dimensions) that were distributed uniformly over a Gaussian shaped hill surface. In RAMI-3 a nontopography version of the same coniferous forest was added in order to investigate whether the deviations in the RT simulations in the Gaussian hill scenario were solely due to the topography itself. Both implementations of the "conifer forest" feature identical numbers and sizes of trees. Figure 15 displays the model simulated BRFs in the principal (first and second rows) and orthogonal (third and fourth rows) viewing planes for the "conifer forest" scene with topography (Figure 15, left), without topography (Figure 15, middle), and the difference between these two (Figure 15, right). Simulations pertain to the red (first and third row) and near-infrared (second and fourth row) spectral regimes of the canopy, and $\theta_i = 40°$.

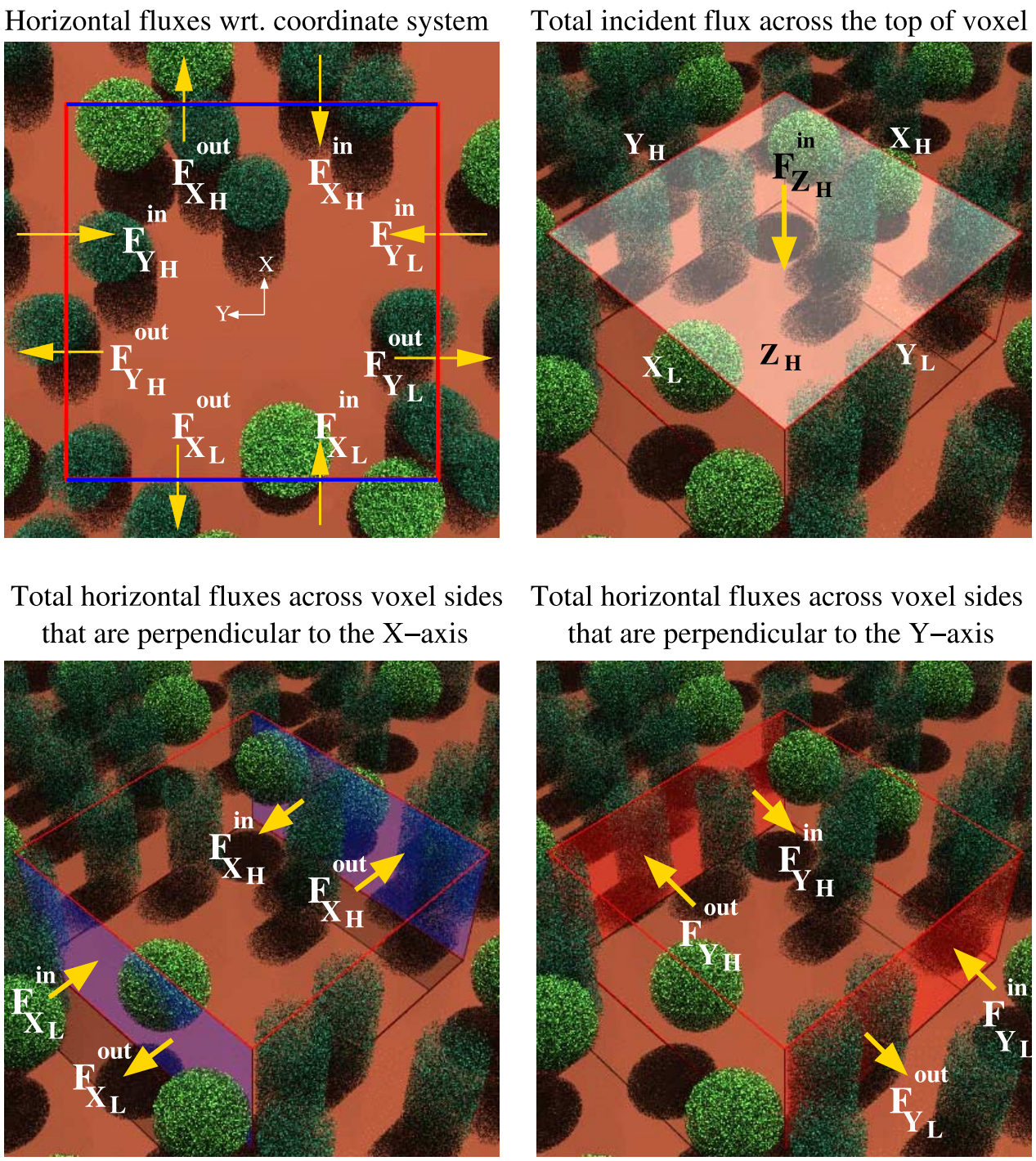

Figure 13. Schematics of the various horizontal (and incident) total fluxes entering and exiting a voxel, here of 30 × 30 × 15 m lateral dimensions, via its lateral (and top) sides. Note that the *x* axis is aligned with the azimuthal direction of the incident light.

[42] One notices the close agreement between the BRF simulations of the models drat, Rayspread, raytran, and Sprint3 in all of the test cases. The MAC model provided identical simulations for both the flat background and the Gaussian hill scenarios. Both of these tend to be higher than the BRF values from most other models, however. The 5Scale model, which utilizes a cylinder and a cone to represent the shape of the tree crowns, generates somewhat higher BRF values in the red spectral domain and somewhat lower BRF values in the NIR spectral domain. Accounting for the reduced number of models participating in the Gaussian hill case, one may say that, overall, the envelope of all the BRF simulations in the Gaussian hill scenario is very similar to that in the flat background case. The impact of topography becomes, however, noticeable when subtracting the BRF simulations in the flat background case from those of the corresponding Gaussian hill scenario (right column), in particular at large view zenith angles. For

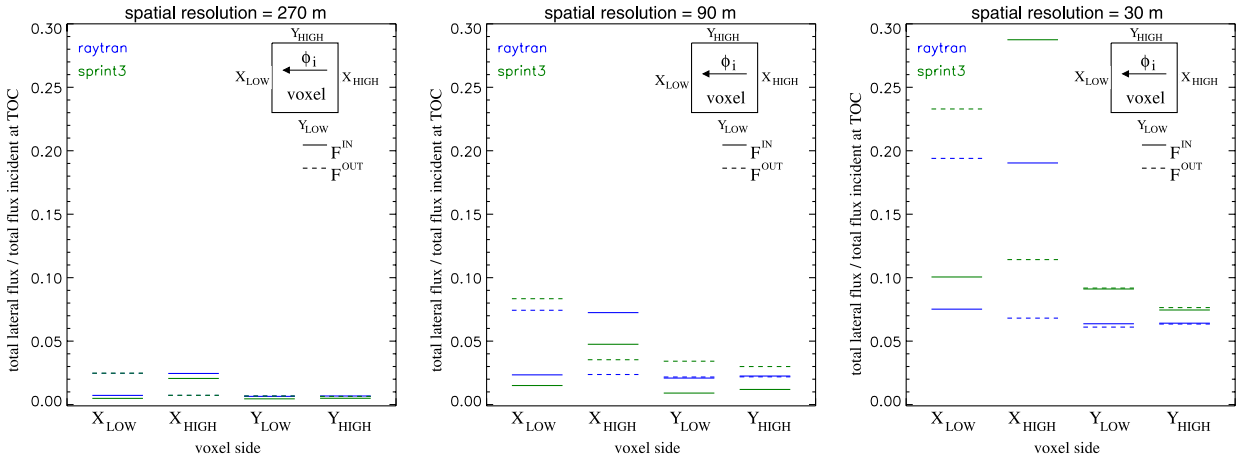

Figure 14. Normalized horizontal fluxes entering (solid) and exiting (dashed) the lateral sides of voxels with spatial dimensions equal to (left) 270 m, (middle) 90 m, and (right) 30 m in the NIR spectral domain. The voxels are centered at the origin of the local coordinate system and have a height of 15 m. The illumination azimuth, ϕ_i, is parallel (perpendicular) to the voxel sides labeled Y_{LOW} and Y_{HIGH} (X_{LOW} and X_{HIGH}), and $\theta_i = 20°$.

observations close to nadir, on the other hand, few topography-induced differences can be observed since both "conifer forest" representations feature identical canopy statistics (e.g., LAI, tree number, fractional cover, etc.). In the principal plane the presence of a hill shaped background thus leads to enhanced BRFs in the backward scattering direction (i.e., a large amount of radiation is reflected back from the illuminated slopes of the hill), and reduced BRFs in the forward scattering direction (i.e., little reflection from that part of the scene that lies in the shadow of the hill). In the orthogonal plane, the Gaussian hill BRFs exceed those of the flat background case at large view zenith angles because of the larger contribution from the snowy slopes of the Gaussian hill (i.e., the single-uncollided BRF component). In the NIR, this effect is somewhat dampened by the single-collided and multiple-collided BRF components, which tend to be larger in the flat background case. The absolute impact that the Gaussian hill exerts on the simulated BRFs thus tends to be more noticeable in the red than the NIR spectral regime.

4.4. "Floating Spheres" Purist Corner

[43] Adding conservative scattering conditions in heterogeneous canopy environments allows to push the RT formulations of 3-D models to their limits, in particular with respect to the multiple scattered radiation component. RAMI-3 thus proposed to run the "floating spheres" test cases under purist corner conditions, i.e., with $r_l = t_l = 0.5$ and $\alpha = 1$. Seven RT models participated in these test cases and their simulation results are shown in Figure 16. More specifically, the total BRFs in the principal (Figure 16, left) and orthogonal (Figure 16, right) planes for discrete (Figure 16, top) and turbid medium (Figure 16, bottom) "floating spheres" representations at two different illumination zenith angles ($\theta_i = 20°$ and 50°) under purist corner conditions are shown. The structure of the scenes is indicated in the inlaid images. One can see that, similar to the solar domain simulations, the 3-D Monte Carlo models drat, Rayspread, raytran, and Sprint3 generated very similar results, with both DART and FRT being somewhat different in the turbid and discrete cases. The 4SAIL2 model, on the other hand, generates significantly higher BRFs than the other models.

4.5. Overall Model Performances in RAMI-3

[44] There is an expectation that the RAMI activity should provide an overall indication of the performance of a given model. This is, however, not a trivial task, since there is a need to account for the reliability of the model simulations, the number of experiments performed, and the computer processing time that was required to do these simulations. Instead, Figure 17 provides an overview of the participation and model-to-ensemble performance of the various models that contributed toward RAMI-3. Statistics are provided for total BRF simulations over structurally homogeneous (Figure 17, top) and heterogeneous (Figure 17, bottom) discrete canopy representations. The various model names are listed on the top of each table (one per column). The experiment identifier is provided to the left, whereas the spectral regime is indicated to the right of each table column. Light (dark) grey fields indicate incomplete (no) data submission. The green-yellow-red color scheme represents the overall model-to-ensemble difference, $\bar{\delta}_m$ quantifying the dispersion that exists between a given model m and all other models that have performed the complete set of prescribed total BRF simulations for the experiment/spectral regime combination of interest. One will note that almost all models, whether analytic, stochastic, hybrid, or Monte Carlo, agree to within 2–4% with the ensemble of all other models in the homogeneous cases. The MBRF model stands out as being somewhat different from the other RAMI-3 participants. In the heterogeneous case, the 3-D MC models tend to be in good agreement with the ensemble of model simulations, whereas models with structural and radiative approximations/parameterisations deviate somewhat more, as was discussed and documented in the various previous subsections. One should note that the predominant hue in the $\bar{\delta}_m$ colors of any given row in Figure 17 depends both on the degree and manner in which the models are

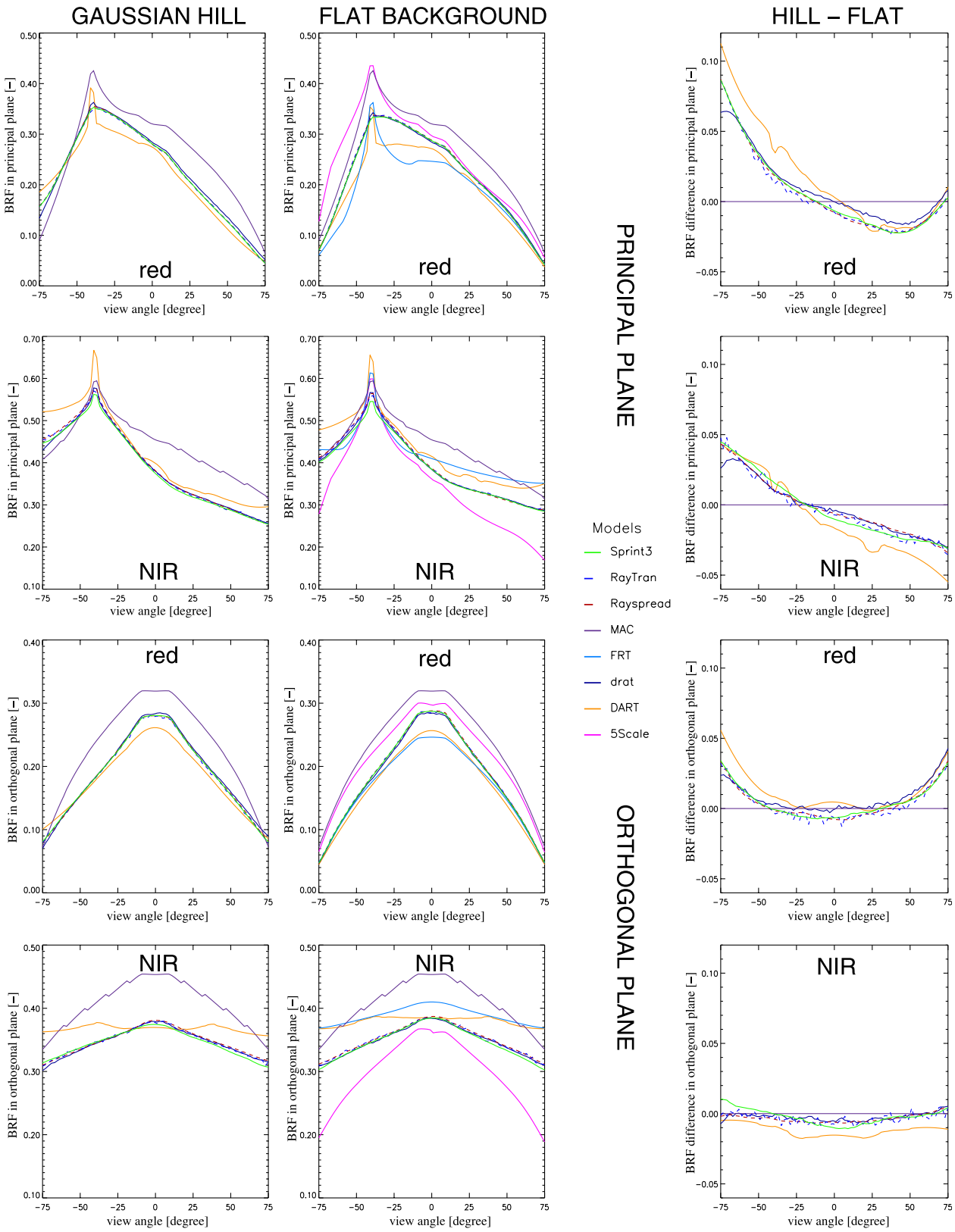

Figure 15. Model simulated BRFs in the principal (first and second rows) and orthogonal (third and fourth rows) viewing planes for the "conifer forest" scene (left) with topography, (middle) without topography, as well as (right) the difference between these two, respectively. Simulations pertain to the red (first and third row) and near-infrared (second and fourth row) spectral regimes at $\theta_i = 40°$.

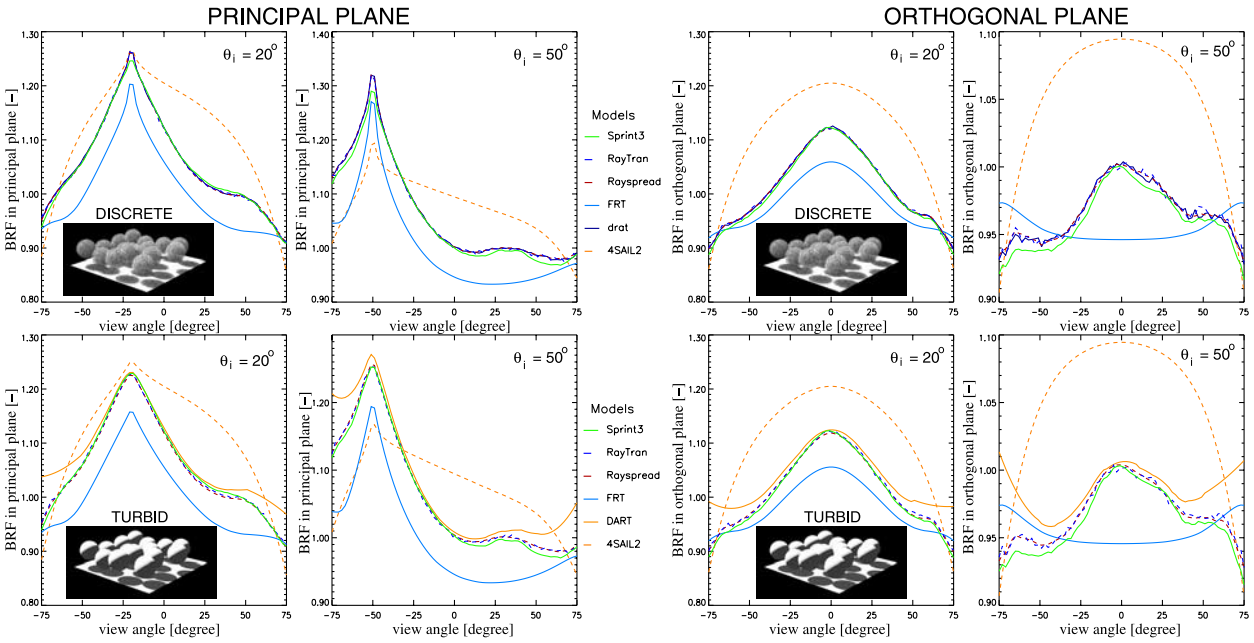

Figure 16. Model simulated BRFs for the "floating spheres scene under conservative scattering conditions (purist corner). Results are shown in the (left) principal and (right) orthogonal observation planes for (top) discrete and (bottom) turbid medium foliage representations and two different illumination zenith angles (θ_i). The structure of the scenes is indicated in the inlaid images.

dispersed around the main cluster of simulation results. The mostly red colors characterizing $\bar{\delta}_m$ for the discrete "floating spheres" canopies in the NIR spectral domain (second to last row in Figure 17, bottom), for example, are due to the consistently large deviations of the 5Scale and 4SAIL2 simulations with respect to each other and to the cluster of 3-D Monte Carlo models. Finally, the large and noticeable amount of (light and dark) grey patches in Figure 17 indicates that a significant number of experiments were not completed or submitted.

5. Concluding Remarks

[45] The third phase of the RAdiation transfer Model Intercomparison (RAMI) activity with its record participation, its extensive set of new experiments and measurements, and its substantially improved agreement between 3-D MC models sets a milestone in the evolution of the RT modeling community. It is now estimated that about 60–65% of all currently existing canopy reflectance models have voluntarily participated at some time or other in the RAMI initiative. Through its continuing support and active encouragement of RAMI the RT modeling community has demonstrated maturity (1) by acknowledging the necessity for quality assured RT models if these are to be applied to the interpretation of remotely sensed data, (2) by voluntarily contributing to the establishment of benchmarking scenarios against which future developments of RT models may be evaluated, and (3) by agreeing to publish their model simulations in the refereed scientific literature prior to knowing the results of the intercomparison exercise. Since its first phase in 1999, RAMI has served as a vehicle to document the performance of the latest generation of RT models by charting both their capabilities and weaknesses under a variety of spectral and structural conditions. During RAMI-3 it has been possible to actually demonstrate, for the first time, a general convergence of the ensemble of submitted RT simulations (with respect to RAMI-2), and to document the unprecedented level of agreement that now exists between the participating 3-D Monte Carlo models. These positive developments do not only further the confidence that may be placed in the quality of canopy reflectance models, but they also pave the way for addressing new and challenging issues, most notably, in the context of supporting field validation efforts of remotely sensed products. The latter is of prime importance given the abundance of global surface products from the current fleet of instruments, like MISR, MODIS, MERIS, etc. The usage of quality-assured RT models in detailed simulations of in situ field measurements at very high spatial resolutions is thus only a first step toward proposing optimal sampling/upscaling schemes that guarantee accurate domain-averaged absorption, transmission, etc. estimates. RAMI-3 has, however, also shown that only a few models are currently able to perform such kinds of RT simulations. The challenge thus lies with the modeling community as a whole to provide the scientists involved in field validation campaigns of satellite derived surface products with optimal sampling practices that are rooted in a proper understanding of the radiative transfer in architecturally complex 3-D media.

5.1. Structurally Divergent Model Premises

[46] More models than ever participated in the third phase of RAMI, and the agreement between them, in particular for the various baseline scenarios, has noticeably increased with respect to previous phases of RAMI (Figure 7). The continuation of the strategy adopted during RAMI-2, i.e., to provide detailed descriptions of the position and orientation of every single leaf in scenes with discrete foliage representations, as well as indications of all tree/crown

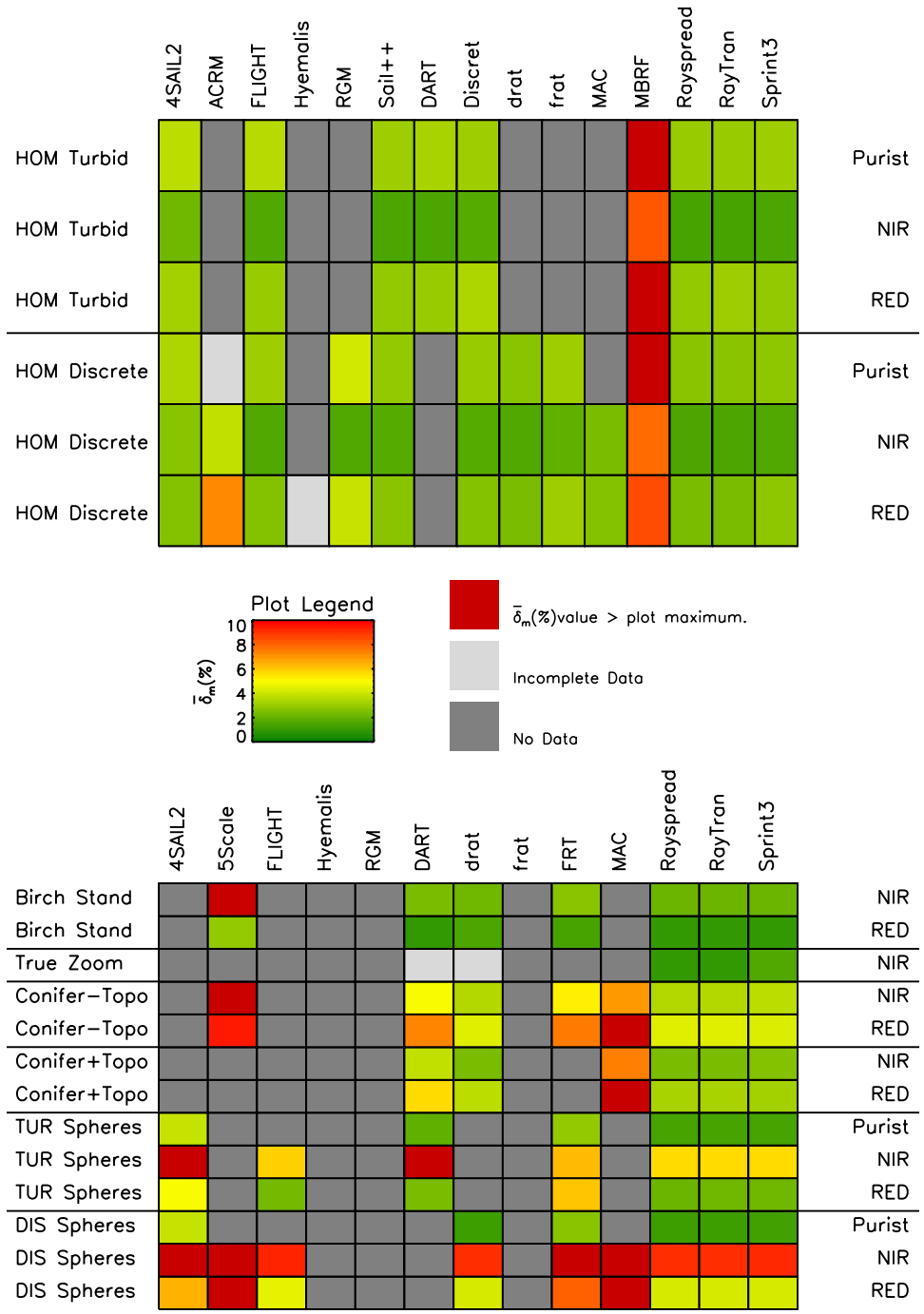

Figure 17. Model performance and participation during RAMI-3 for structurally (top) homogeneous and (bottom) heterogeneous discrete canopy representation. Model names are listed on the top of each table (one per column). The experiment identifier is provided to the left and the spectral regime is provided to the right of each table column. Light (dark) grey fields indicate incomplete (no) data submission. The green-yellow-red color scheme represents the integrated model-to-ensemble difference, $\bar{\delta}$ [%] obtained with respect to all models that have performed the complete set of prescribed total BRF simulations for any given experiment/spectral regime combination.

locations in the relevant scenes on the RAMI Web site, has, among other factors, contributed to improving the agreement among the various 3-D MC RT models (Figures 6, 8, 10, and 16 and Table 2). This development provides further weight to using these models in defining a "surrogate truth" that may then be used, even for structurally heterogeneous canopy architectures, to obtain an indication of the performance of other RT models. It may be argued, however, that such an approach is only meaningful if all the models implement identical canopy representations in their RT simulations. Both the deviations in the structural premises of a RT model and the approximations and/or errors in the

implementation of the model's radiative transfer formulation may be held responsible for the observed BRF/flux differences. If the purpose of RAMI were solely to identify RT related differences in canopy reflectance models, then the current flexibility in the implementation of RAMI test cases would have to be replaced by rigorously specified canopy architectures that were specifically tailored to the scene description formalism of each and every participating RT model. Alternatively, the derivation and use of "effective" state variables may be proposed to potential RAMI participants, since recent findings [e.g., *Cairns et al.*, 2000; *Pinty et al.*, 2006; *Widlowski et al.*, 2005], have suggested that diverging target structures may still yield identical radiative properties provided that "effective" instead of actual state variable values are available for RT simulations (one possible approach to derive such effective state variables is described by *Pinty et al.* [2004a]).

[47] Ultimately, however, it is the accuracy of the retrieved state variable values that counts in RT model applications. The logical consequence of this line of reasoning thus would be to address the inversion of RT models in the context of RAMI against predefined sets of spectral and angular observations, similar to those provided by the current fleet of space borne sensors, e.g., ATSR-2/AATSR [*Stricker et al.*, 1995], CHRIS-Proba [*Barnsley et al.*, 2004], MISR [*Diner et al.*, 2002], and POLDER [*Deschamps et al.*, 1994]. In this way, the impact that the various structural and radiative formalisms in the RT models may have with respect to the values of the retrieved state variables could then be assessed in the light of the known uncertainties in the available surface BRFs. Indeed, during RAMI-1 a set of "inverse mode" scenarios had been proposed but this had been abandoned in subsequent phases because of a lack of participants. Given the close agreement of the various participating models in RAMI-3, it may become appropriate to revisit this issue in the future.

5.2. RAMI Online Model Checker (ROMC)

[48] One of the positive outcome of RAMI-3 is the consistently good agreement (see Table 2) between simulation results of a small set of 3-D MC models, and this both over homogeneous as well as heterogeneous vegetation canopies. It is thus feasible to derive a "surrogate truth" for almost all of the measurements and experiments featured within RAMI (current exceptions are the "local transmission transects," the "local horizontal fluxes" and some of the BRF simulations relating to the 30 m spatial resolution patches in the "true zoom-in" experiment). With this valuable data set at hand, it becomes possible to allow model owners, developers and customers to evaluate the performance of a given RT model even outside the frame of a RAMI phase. To facilitate such an undertaking the RAMI Online Model Checker (ROMC) was developed at the Joint Research Centre of the European Commission in Ispra, Italy. The ROMC is a web-based interface allowing for the online evaluation of RT models using as reference the "surrogate truth" derived from among the 6 Monte Carlo models DART, drat, FLIGHT, Rayspread, raytran and Sprint3 using an appropriate set of selection criteria (see section 3.3.3). Access to the ROMC can be obtained either via the RAMI Web site or directly using the URL http://romc.jrc.it/. Note that because of a renaming of all European Commission Web sites this URL is likely to change in the near future to http://rami-benchmark.jrc.ec.europa.eu/. After providing a username and valid email address, the ROMC can be utilized in two different ways: (1) in debug mode, which allows to repeatedly compare the output of a RT model to that of one or more experiments and/or measurements from RAMI, i.e., the simulation results are available on the RAMI Web site, and (2) in validate mode, which enables the once-only testing of the RT model against a continuously changing set of test cases that are similar but not quite equivalent to those from RAMI, i.e., the solutions are not known a priori and the experiments cannot be repeated.

[49] 1. In debug mode users may choose to execute one particular experiment and/or measurement from the set of RAMI-3 test cases ad infinitum, or, at least until they are satisfied with the performance of their model. Detailed descriptions of the structural, spectral, illumination and measurement conditions are available. Once the model simulation results are generated, they can be uploaded via the web-interface, and, provided they adhere to the RAMI filenaming and formatting conventions, this process will result in a series of graphical results files being made available for all test cases. In debug mode users may not only download their ROMC results but also an ASCII file containing the actual "surrogate truth" data.

[50] 2. In validate mode users may choose between structurally homogeneous and/or heterogeneous "floating spheres" canopies to verify the performance of their model. The actual set of test cases will, however, be drawn randomly from a large list of possible ones, such that it is unlikely to obtain the same test case twice, i.e., in all likelihood one will not "know" the solution a priori. Again, the "surrogate truth" was derived from simulations generated by models belonging to the same set of 3-D MC models as was the case for the debug mode. In validate mode the reference data will, however, not be available for downloading. The procedure for data submission, on the other hand, is identical to that of the debug mode, and, provided that all RAMI formatting and filenaming requirements were applied, will also lead to a results page featuring a variety of intercomparison graphics.

[51] Users may download their ROMC results either as jpeg formatted images from the ROMC Web site, or else, opt for receiving them via email in postscript form. Both the debug and validate mode ROMC results files feature a reference number. Available graphs include: Plots of both the model and reference BRFs in the principal or orthogonal plane, 1 to 1 plots of the model and reference BRFs, histograms of the deviations between model and reference BRFs, χ^2 graphs for all submitted measurements using an f value of 3% as well as graphs depicting the deviation of the model and reference fluxes using barcharts. Users of ROMC are encouraged to utilize only ROMC results that were obtained in validate mode for publications. Those obtained in debug mode, obviously, do not qualify as proof regarding the performance of a RT model since all simulation results may readily be viewed on the RAMI Web site. Last but not least, a large ensemble of FAQs should help to guide the user through the ROMC applications. It is hoped that the ROMC will prove useful for the RT modeling community, not only by providing a convenient means to evaluate RT models outside the triennial phases of RAMI

(something that was rather tedious in the past if authors wished to rely on the experiences gained from RAMI [e.g., *Gastellu-Etchegorry et al.*, 2004]) but also to attract participation in future RAMI activities.

5.3. Future Perspectives for RAMI

[52] RAMI was conceived as an open-access community exercise and will continue to pursue that direction. As such its goal is to move forward in a manner that addresses the needs of the majority of RT model (developers and users). For example, relatively simple RT modeling approaches designed only to simulate integrated fluxes, like the 2-Stream model, should not be neglected in future developments of RAMI due the large communities involved with soil-vegetation-atmosphere transfer (SVAT) models, as well as general circulation models. Whereas such two stream approaches remove all dependencies on vegetation structure beyond leaf quantity and orientation, the various findings of RAMI-3, and in particular the above discussion, have highlighted the relevance of canopy structure in forward mode RT simulations. With every model having its own implementation of "reality" it may be appropriate to provide as detailed descriptions as possible of highly realistic canopy architectures in future phases of RAMI [e.g., *Disney et al.*, 2006]. Various techniques are currently available for the generation of realistic 3-D trees, the most well known one being probably the L-systems approach [e.g., *Prusinkiewicz and Lindenmayer*, 1990; *Weber and Penn*, 1995; *De Reffye and Houllier*, 1997]. Using these methodologies to generate a detailed depiction of the architectural characteristics of (part of) well documented sites, like BOREAS [*Sellers et al.*, 1997] and/or the Kalahari transect (SAFARI 2000) [*Scholes et al.*, 2004], for example, would allow one to (1) study the variability in the radiative surface properties predicted by a whole suite of participating RT models, as well as their possible impact on the hydrological and carbon cycles; (2) investigate by how much RT model simulations vary when carried out on the basis of canopy representations with a progressively increasing degree of structural abstractions (all state variable values remain constant, or are converted to "effective" values) [e.g., *Pinty et al.*, 2004a; *Smolander and Stenberg*, 2005; *Rochdi et al.*, 2006]; (3) compare such surface BRF simulations with atmospherically corrected observations from space borne instruments; (4) investigate the potential of RT models to reproduce in situ measurements of transmitted light, e.g., Tracing Radiation and Architecture of Canopies (TRAC) instrument [*Chen and Cihlar*, 1995; *Leblanc*, 2002], and/or hemispherical photographs [*Leblanc et al.*, 2005; *Jonckheere et al.*, 2005]; and (5) assess the accuracy of upscaling methodologies currently used in validation efforts of satellite derived products like FAPAR and LAI [e.g., *Morisette et al.*, 2006]. In this way RAMI can actively contribute toward systematic validation efforts of RT models, operational algorithms, and field instruments, as promoted by the Committee on Earth Observation Satellites (CEOS).

[53] **Acknowledgments.** The definition of the RAMI test cases on a dedicated Web site, the coordination of the RAMI participants, and the analysis of the submitted simulation results would not have been possible without the financial support of the European Commission and, more specifically, the Global Environment Monitoring unit of the Institute for Environment and Sustainability in the DG Joint Research Centre. The valuable comments of the three anonymous reviewers and the stimulating exchanges with the various scientists of the RAMI Advisory Body (RAB), as well as those involved with the I3RC, are also gratefully acknowledged.

References

Barnsley, M. J., J. J. Settle, M. Cutter, D. Lobb, and F. Teston (2004), The PROBA/CHRIS mission: A low-cost smallsat for hyperspectral, multi-angle, observations of the Earth surface and atmosphere, *IEEE Trans. Geosci. Remote Sens.*, *42*, 1512–1520.

Bruegge, C. J., N. L. Chrien, R. R. Ando, D. J. Diner, W. A. Abdou, M. C. Helmlinger, S. H. Pilorz, and K. J. Thome (2002), Early validation of the Multi-angle Imaging SpectroRadiometer (MISR) radiometric scale, *IEEE Trans. Geosci. Remote Sens.*, *40*, 1477–1492.

Bunnik, N. J. J. (1978), The multispectral reflectance of shortwave radiation of agricultural crops in relation with their morphological and optical properties, *Tech. Rep. 707*, Mededelingen Landbouwhogeschool, Wageningen, Netherlands.

Cahalan, R. F., et al. (2005), The international intercomparison of 3D radiation codes (I3RC): Bringing together the most advanced radiative transfer tools for cloudy atmospheres, *Bull. Am. Meteorol. Soc.*, *86*, 1275–1293.

Cairns, B., A. Lacis, and B. Carlson (2000), Absorption within inhomogeneous clouds and its parameterization in general circulation models, *J. Atmos. Sci.*, *57*, 700–714.

Campbell, G. S. (1990), Derivation of an angle density function for canopies with ellipsoidal leaf angle distribution, *Agric. For. Meteorol.*, *49*, 173–176.

Chen, J. M., and J. Cihlar (1995), Plant canopy gap size analysis theory for improving optical measurements of leaf area index, *Appl. Opt.*, *34*, 6211–6222.

Chen, J. M., J. Liu, S. G. Leblanc, R. Lacaze, and J. L. Roujean (2003), Multi-angular optical remote sensing for assessing vegetation structure and carbon absorption, *Remote Sens. Environ.*, *84*, 516–525.

Chopping, M. J., A. Rango, K. M. Havstad, F. R. Schiebe, J. C. Ritchie, T. J. Schmugge, A. N. French, L. Su, L. McKee, and R. Davis (2003), Canopy attributes of desert grasslands and transition communities derived from multi-angular airborne imagery, *Remote Sens. Environ.*, *85*, 339–354.

De Reffye, P., and F. Houllier (1997), Modelling plant growth and architecture: Some recent advances and applications to agronomy and forestry, *Curr. Sci.*, *73*, 984–992.

Deschamps, P. Y., F.-M. Bréon, M. Leroy, A. Podaire, A. Bricaud, J.-C. Buriez, and G. Sèze (1994), The POLDER mission: Instruments characteristics and scientifc objectives, *IEEE Trans. Geosci. Remote Sens.*, *32*, 586–615.

Diner, D. J., J. C. Beckert, G. W. Bothwell, and J. I. Rodrigues (2002), Performance of the MISR instrument during its first 20 months in Earth orbit, *IEEE Trans. Geosci. Remote Sens.*, *40*, 1449–1466.

Dirmeyer, P. A., A. J. Dolman, and N. Sato (1999), The global soil wetness project: A pilot project for global land surface modeling and validation, *Bull. Am. Meteorol. Soc.*, *80*, 851–878.

Disney, M. I., P. Lewis, and P. R. J. North (2000), Monte Carlo raytracing in optical canopy reflectance modelling, *Remote Sens. Rev.*, *18*, 163–196.

Disney, M. I., P. Lewis, and P. Saich (2006), 3D modelling of forest canopy structure for remote sensing simulations in the optical and microwave domains, *Remote Sens. Environ.*, *100*, 114–132.

Fernandes, R. A., S. G. Leblanc, and A. Simic (2003), A multi-scale analytical canopy (MAC) reflectance model based on the angular second order gap size distribution, *Proc. Int. Geosci. Remote Sens. Symp.*, *7*, 4431–4433.

Gastellu-Etchegorry, J.-P., V. Demarez, V. Pinel, and F. Zagolski (1996), Modeling radiative transfer in heterogeneous 3-D vegetation canopies, *Remote Sens. Environ.*, *58*, 131–156.

Gastellu-Etchegorry, J.-P., E. Martin, and F. Gascon (2004), Dart: A 3D model for simulating satellite images and studying surface radiation budget, *Int. J. Remote Sens.*, *25*, 73–96.

Gates, W. L., et al. (1998), An overview of the results of the atmospheric model intercomparison project (AMIP I), *Bull. Am. Meteorol. Soc.*, *73*, 1962–1970.

Gerard, F. F., and P. R. J. North (1997), Analyzing the effect of structural variability and canopy gaps on forest BRDF using a geometric-optical model, *Remote Sens. Environ.*, *62*, 46–62.

Gerstl, S. A. W. (1988), Angular reflectance signature of the canopy hotspot in the optical regime, in *4th International Colloquium on Spectral Signatures of Objects in Remote Sensing*, *Aussois*, *France*, *Eur. Space Agency Spec. Publ.*, *ESA SP-287*, 129.

Gobron, N., B. Pinty, M. M. Verstraete, and Y. Govaerts (1997), A semi-discrete model for the scattering of light by vegetation, *J. Geophys. Res.*, *102*, 9431–9446.

Gobron, N., et al. (2006), Evaluation of FAPAR products for different canopy radiation transfer regimes: Methodology and results using JRC products derived from SeaWiFS against ground-based estimations, *J. Geophys. Res.*, *111*, D13110, doi:10.1029/2005JD006511.

Goel, N. S., and D. E. Strebel (1984), Simple beta distribution representation of leaf orientation in vegetation canopies, *Agron. J.*, *76*, 800–803.

Govaerts, Y., and M. M. Verstraete (1998), Raytran: A Monte Carlo ray tracing model to compute light scattering in three-dimensional heterogeneous media, *IEEE Trans. Geosci. Remote Sens.*, *36*, 493–505.

Halthore, R. N., et al. (2005), Intercomparison of shortwave radiative transfer codes and measurements, *J. Geophys. Res.*, *110*, D11206, doi:10.1029/2004JD005293.

Helbert, J., B. Berthelot, and C. Soler (2003), Hyemalis: Un simulateur d'images de paysages tridimensionnels complexes, in *Revue Française de Photogrammétrie et de Télédétection*, vol. 173/174, pp. 27–35, Soc. Fr. de Photogramm. et de Télédétection, Marne la Vallée, France.

Henderson-Sellers, A., A. J. Pitman, P. K. Love, P. Irannejad, and T. Chen (1995), The project for intercomparison of land surface parameterisaton schemes (PILPS): Phases 2 and 3, *Bull. Am. Meteorol. Soc.*, *76*, 489–503.

Jonckheere, I., B. Muys, and P. Coppin (2005), Assessment of automatic gap fraction estimation of forests from digital hemispherical photography, *Agric. For. Meteorol.*, *132*, 96–114.

Kneubühler, M., M. Schaepman, K. Thome, F. Baret. and A. Müller (2002), Calibration and validation of Envisat MERIS. Part 1: Vicarious calibration at Rail Road valley Playa (NV), paper presented at MERIS Level 2 validation Workshop, ESRIN, Frascati, Italy, 9–13 Dec.

Kuusk, A. (1991), The hot spot effect in plant canopy reflectance, in *Photon-Vegetation Interactions*, edited by R. Myneni and J. Ross, pp. 139–159, Springer, New York.

Kuusk, A. (2001), A two-layer canopy reflectance model, *J. Quant. Spectrosc. Radiat. Transfer*, *71*, 1–9.

Kuusk, A., and T. Nilson (2000), A directional multispectral forest reflectance model, *Remote Sens. Environ.*, *72*, 244–252.

Latif, M., et al. (2001), ENSIP: The El Niño simulation intercomparison project, *Clim. Dyn.*, *18*, 255–276.

Leblanc, S. G. (2002), Correction to the plant canopy gap size analysis theory used by the Tracing Radiation and Architecture of Canopies (TRAC) instrument, *Appl. Opt.*, *31*, 7667–7670.

Leblanc, S. G., and J. M. Chen (2001), A windows graphic user interface (GUI) for the five-scale model for fast BRDF simulations, *Remote Sens. Rev.*, *19*, 293–305.

Leblanc, S. G., J. M. Chen, R. Fernandes, D. W. Deering, and A. Conley (2005), Methodology comparison for canopy structure parameters extraction from digital hemispherical photography in boreal forests, *Agric. For. Meteorol.*, *129*, 187–207.

Lewis, P. (1999), Three-dimensional plant modelling for remote sensing simulation studies using the botanical plant modelling system, *Agron. Agric. Environ.*, *19*, 185–210.

Lovell, J. L., and R. D. Graetz (2002), Analysis of POLDER-ADEOS data for the Australian continent: The relationship between BRDF and vegetation structure, *Int. J. Remote Sens.*, *23*, 2767–2796.

Morisette, J. T., et al. (2006), Validation of global moderate resolution LAI products: A framework proposed within the CEOS Land Product Validation subgroup, *IEEE Trans. Geosci. Remote Sens.*, *44*, 1804–1817.

North, P. R. J. (1996), Three-dimensional forest light interaction model using a Monte Carlo method, *IEEE Trans. Geosci. Remote Sens.*, *34*, 946–956.

Oreskes, N., K. Shrader-Frechette, and K. Belitz (1994), Verification, validation, and confirmation of numerical models in the earth sciences, *Science*, *263*, 641–646.

Pinty, B., et al. (2001), The Radiation Transfer Model Intercomparison (RAMI) exercise, *J. Geophys. Res.*, *106*, 11,937–11,956.

Pinty, B., N. Gobron, J.-L. Widlowski, T. Lavergne, and M. M. Verstraete (2004a), Synergy between 1-D and 3-D radiation transfer models to retrieve vegetation canopy properties from remote sensing data, *J. Geophys. Res.*, *109*, D21205, doi:10.1029/2004JD005214.

Pinty, B., et al. (2004b), The Radiation Transfer Model Intercomparison (RAMI) exercise: Results from the second phase, *J. Geophys. Res.*, *109*, D06210, doi:10.1029/2003JD004252.

Pinty, B., T. Lavergne, R. E. Dickinson, J.-L. Widlowski, N. Gobron, and M. M. Verstraete (2006), Simplifying the interaction of land surfaces with radiation for relating remote sensing products to climate models, *J. Geophys. Res.*, *111*, D02116, doi:10.1029/2005JD005952.

Prusinkiewicz, P., and A. Lindenmayer (1990), *The Algorithmic Beauty of Plants*, 240 pp., Springer, New York.

Qin, W., and S. A. W. Gerstl (2000), 3-D scene modeling of semi-desert vegetation cover and its radiation regime, *Remote Sens. Environ.*, *74*, 145–162.

Qin, W., and Y. Xiang (1997), An analytical model for bidirectional reflectance factor of multicomponent vegetation canopies, *Sci. China, Ser. C*, *40*, 305–315.

Rautiainen, M., P. Stenberg, T. Nilson, and A. Kuusk (2003), The effect of crown shape on the reflectance of coniferous stands, *Remote Sens. Environ.*, *89*, 41–52.

Rochdi, N., R. Fernandes, and M. Chelle (2006), An assessment of needles clumping within shoots when modeling radiative transfer within homogeneous canopies, *Remote Sens. Environ.*, *102*, 116–135.

Ross, J. (1981), *The Radiation Regime and Architecture of Plant Stands*, Springer, New York.

Saich, P., P. Lewis, M. Disney, and G. Thackrah (2001), Comparison of Hymap/E-SAR data with models for optical reflectance and microwave scattering from vegetation canopies, in *3rd International Symposium on Retrieval of Bio- and Geophysical Parameters From SAR data for Land Applications (LANDSAR 2001)*, *Eur. Space Agency Spec. Publ.*, *ESA-SP 475*.

Scholes, R. J., P. G. H. Frost, and Y. Tian (2004), Canopy structure in savannas along a moisture gradient on Kalahari sands, *Global Change Biol.*, *10*, 292–302, doi:10.1111.

Sellers, P. J., et al. (1997), BOREAS in 1997: Experiment overview, scientific results and future directions, *J. Geophys. Res.*, *102*, 28,731–28,770.

Shultis, J. K., and R. B. Myneni (1988), Radiative transfer in vegetation canopies with anisotropic scattering, *J. Quant. Spectrosc. Radiat. Transfer*, *39*, 115–129.

Smolander, S., and P. Stenberg (2005), Simple parameterizations of the radiation budget of uniform broadleaved and coniferous canopies, *Remote Sens. Environ.*, *94*, 355–363.

Soler, C., and F. Sillion (2000), Hierarchical instantiation for radiosity, in *Rendering Techniques '00*, edited by B. Peroche and H. Rushmeier, pp. 173–184, Springer, New York.

Stricker, N. C. M., A. Hahne, D. L. Smith, and J. Delderfield (1995), ATSR-2: The evolution in its design from ERS-1 to ERS-2, *ESA Bull.*, *83*, 32–37.

Thompson, R. L., and N. S. Goel (1998), Two models for rapidly calculating bidirectional reflectance: Photon spread (ps) model and statistical photon spread (sps) model, *Remote Sens. Rev.*, *16*, 157–207.

Tian, Y., Y. Wang, Y. Zhang, Y. Knyazikhin, J. Bogaert, and R. B. Myneni (2002), Radiative transfer based scaling of LAI retrievals from reflectance data of different resolutions, *Remote Sens. Environ.*, *84*, 143–159.

Verhoef, W. (1998), Theory of radiative transfer models applied to optical remote sensing of vegetation canopies, Ph.D. thesis, Wageningen Agric. Univ., Wageningen, Netherlends.

Verhoef, W. (2002), Improved modelling of multiple scattering in leaf canopies: The model SAIL++, in *Proceedings of the First Symposium on Recent Advances in Quantitative Remote Sensing, Torrent, Spain, September 2002*, edited by A. Sobrino, pp. 11–20, Serv. de Publ. Univ. de Valencia, Valencia, Spain.

Verhoef, W., and H. Bach (2003), Simulation of hyperspectral and directional radiance images using coupled biophysical and atmospheric radiative transfer models, *Remote Sens. Environ.*, *87*, 23–41.

Verstraete, M. M. (1987), Radiation transfer in plant canopies: Transmission of direct solar radiation and the role of leaf orientation, *J. Geophys. Res.*, *92*, 10,985–10,995.

Verstraete, M. M. (1988), Radiation transfer in plant canopies: Scattering of solar radiation and canopy reflectance, *J. Geophys. Res.*, *93*, 9483–9494.

Weber, J., and J. Penn (1995), Creation and rendering of realistic trees, in *Proceedings of the 22nd Annual Conference on Computer Graphics and Interactive Techniques*, pp. 119–128, ACM Press, New York.

Widlowski, J.-L., B. Pinty, N. Gobron, M. M. Verstraete, and A. B. Davis (2001), Characterization of surface heterogeneity detected at the MISR/TERRA subpixel scale, *Geophys. Res. Lett.*, *28*, 4639–4642.

Widlowski, J.-L., B. Pinty, T. Lavergne, M. M. Verstraete, and N. Gobron (2005), Using 1-D models to interpret the reflectance anisotropy of 3-D canopy targets: Issues and caveats, *IEEE Trans. Geosci. Remote Sens.*, *43*, 2008–2017, doi:10.1109/TGRS.2005.853718.

Widlowski, J.-L., T. Lavergne, B. Pinty, M. M. Verstraete, and N. Gobron (2006a), Rayspread: A virtual laboratory for rapid BRF simulations over 3-D plant canopies, in *Computational Methods in Transport*, *Lecture Notes in Comput. Sci. and Eng. Ser.*, vol. 48, edited by G. Frank, pp. 211–231, Springer, New York.

Widlowski, J.-L., B. Pinty, T. Lavergne, M. M. Verstraete, and N. Gobron (2006b), Horizontal radiation transport in 3-D forest canopies at multiple spatial resolutions: Simulated impact on canopy absorption, *Remote Sens. Environ.*, *103*, 379–397, doi:10.1016/j.rse.2006.03.014.

V. Bruniquel-Pinel and R. Ruiloba, NOVELTIS, Parc Technologique du Canal, 2 avenue de l'Europe, F-31520 Ramonville Saint-Agne, France.

M. Disney and P. E. Lewis, Department of Geography, University College London, 26 Bedford Way, London WC1H 0AP, UK.

R. Fernandes and N. Rochdi, Canada Centre for Remote Sensing, Natural Resources Canada, 588 Booth Street, Ottawa, ON, Canada K1A 0Y7.

J.-P. Gastellu-Etchegorry and E. Martin, Centre d'Etudes Spatiales de la Biosphère, 18 av. Edouard Belin, bpi 2801, F-31401 Toulouse cedex 9, France.

N. Gobron, T. Lavergne, B. Pinty, M. Robustelli, M. Taberner, M. M. Verstraete, and J.-L. Widlowski, Global Environment Monitoring Unit, Institute for Environment and Sustainability, European Commission–DG Joint Research Centre, TP 440, via E. Fermi, 1, I-21020 Ispra, Italy. (jean-luc.widlowski@jrc.it)

A. Kuusk and M. Mõttus, Tartu Observatory, 61602 Tõravere, Estonia.

S. Leblanc, Centre Spatial John H. Chapman, 6767, Route de l'Aéroport, Saint-Huber, QC, Canada J3Y 8Y9.

P. R. J. North, Climate and Land-Surface Systems Interaction Centre, Department of Geography, University of Wales, Swansea SA2 8PP, UK.

W. Qin, Science Systems and Applications, Inc., 10210 Greenbelt Road, Suite 600, Lanham, MD 20706, USA.

C. Soler, Acquisition, Representation and Transformations for Image Synthesis, Institut National de Recherche en Informatique et en Automatique Rhône-Alpes, 655, Avenue de l'Europe, F-38334 Saint Ismier Cedex, France.

R. Thompson, Alachua Research Institute, 8202 NW 156 Avenue, P.O. Box 1920, Alachua, FL 32616, USA.

W. Verhoef, National Aerospace Laboratory NLR, P.O. Box 153, NL-8300 AD Emmeloord, Netherlands.

D. Xie, Research Center for Remote Sensing and GIS, School of Geography, Beijing Normal University, No 19 Xinjiekouwai Street, Beijing 100875, China.